

Identifying Mergers Using Quantitative Morphologies in Zoom Simulations of High-Redshift Galaxies

Matthew W. Abruzzo^{1,5*} Desika Narayanan^{2,3,4,5}, Romeel Davé^{6,7,8}
and Robert Thompson⁹

¹*Columbia University, Department of Astronomy, New York, NY 10025, USA*

²*Department of Astronomy, University of Florida, 211 Bryant Space Sciences Center, Gainesville, FL 32611*

³*University of Florida Informatics Institute, 432 Newell Drive, CISE Bldg E251, Gainesville, FL 32611*

⁴*Cosmic Dawn Centre (DAWN), University of Copenhagen, Julian Maries vej 30, DK-2100, Copenhagen, Denmark*

⁵*Department of Physics and Astronomy, Haverford College, 370 Lancaster Ave, Haverford, PA 19041*

⁶*Institute for Astronomy, University of Edinburgh, Royal Observatory, Edinburgh EH9 3HJ, UK*

⁷*University of the Western Cape, Bellville, Cape Town 7925, South Africa*

⁸*South African Astronomical Observatory, Cape Town 7925, South Africa*

⁹*Portalarium, 3410 Far West Blvd, Austin, TX 78731*

Submitted to MNRAS

ABSTRACT

Non-parametric morphology measures are a powerful tool for identifying galaxy mergers at low redshifts. We employ cosmological zoom simulations using GIZMO with the MUFASA feedback scheme, post-processed using 3D dust radiative transfer into mock observations, to study whether common morphological measures Gini G , M_{20} , concentration C , and asymmetry A are effective at identifying major galaxy mergers at $z \sim 2 - 4$, i.e. “Cosmic Noon”. Our zoom suite covers galaxies with $10^{8.6} \lesssim M_* \lesssim 10^{11} M_\odot$ at $z \approx 2$, and broadly reproduces key global galaxy observations. Our primary result is that these morphological measures are unable to robustly pick out galaxies currently undergoing mergers during Cosmic Noon, typically performing no better than a random guess. This improves only marginally if we consider whether galaxies have undergone a merger within the last Gyr. When also considering minor mergers, galaxies display no trend of moving towards the merger regime with increasing merger ratio. From $z = 4 \rightarrow 2$, galaxies move from the non-merger towards the merger regime in all statistics, but this is primarily an effect of mass: Above a given noise level, higher mass galaxies display a more complex outer morphology induced by their clustered environment. We conclude that during Cosmic Noon, these morphological statistics are of limited value in identifying galaxy mergers.

Key words: galaxies: structure – galaxies: formation – methods: numerical

1 INTRODUCTION

A major outstanding question in modern day astronomy is how galaxies form. This question is intimately tied to galaxy morphology. Early on, it was noted that galaxies could be classified by their visual morphology. The Hubble (1926) morphological classification system remains a useful characterisation of galaxies to this day mainly because its morphological classifications are strongly correlated with physical properties: spiral galaxies typically have ongoing star formation and are dominated by the light of bright, bluer, younger stars, whereas elliptical galaxies are usually quiescent and dominated by the light of older, redder, stars

(Conselice 2014). Moreover, within the Λ Cold Dark Matter (Λ CDM) paradigm, dark matter haloes grow hierarchically via mergers (White & Rees 1978; Lacey & Cole 1993; Guo & White 2008), and semi-analytic models of galaxy formation successfully tie the resulting merging process to the morphological evolution of galaxies

Theoretical simulations have demonstrated that major galaxy mergers, canonically defined as having a progenitor mass ratio above 1:4, can have a dramatic effect on the luminosity, structural, and chemical histories of galaxies. Tidal torques from interacting systems can drive gaseous inflows that subsequently fuel intense nuclear starbursts (e.g. Barnes & Hernquist 1992; Mihos & Hernquist 1996; Springel et al. 2005a; Narayanan et al. 2010b; Hopkins et al. 2013; Hayward et al. 2013a, though see Teyssier et al. (2010)).

* E-mail: mwa2113@columbia.edu

This star formation activity can be followed by a period of intense black hole growth (e.g. [Springel et al. 2005a](#); [Hopkins et al. 2005](#); [Younger et al. 2009](#); [Gabor et al. 2016](#)), and eventually result in a “red and dead” elliptical galaxy (e.g. [Springel et al. 2005b](#); [Cox et al. 2008](#)). These processes can have a dramatic impact on the structural and thermal properties of the interstellar medium in galaxies (e.g. [Narayanan et al. 2011, 2012](#)), the kinematic structure of galaxies (e.g. [Cox et al. 2006b](#); [Wuyts et al. 2010](#)), and the formation of stellar bulges ([Hopkins et al. 2009](#)).

In the local Universe, it is clear that the most bolometrically luminous galaxies are principally comprised of mergers. For example, analysis of the morphological structure of infrared-bright galaxies in the local Universe evidenced that the majority of systems forming stars above $\sim 50 M_{\odot}\text{yr}^{-1}$ (or, with infrared luminosities greater than $\sim 10^{11.5} L_{\odot}\text{yr}^{-1}$) owed their origin to major mergers ([Sanders & Mirabel 1996](#); [Veilleux et al. 2002](#); [Casey et al. 2014](#); [Larson et al. 2016](#)). Indeed, surveys of a large sample of relatively local ($z < 0.1$) galaxies show a trend with increasing Luminous Infrared Galaxy ($L_{\text{IR}} > 10^{11} M_{\odot}$) fraction with decreasing pair separation in galaxy mergers ([Ellison et al. 2013](#)).

What is less clear, however, is whether a similar situation holds at higher redshifts. At redshifts $z \lesssim 4$, at a fixed stellar mass, galaxy star formation rates intrinsically increase (e.g. [Rodighiero et al. 2011](#); [Elbaz et al. 2011](#); [Whitaker et al. 2012](#); [Speagle et al. 2014](#)) owing to the strong redshift dependence of the cosmological accretion rate (e.g. [Dekel et al. 2009a](#)). Of these galaxies, dusty infrared-luminous (and often submillimetre-selected) galaxies appear to play a substantial role in contributing to the cosmic star formation rate density (SFRD) ([Le Floch et al. 2005](#); [Dunlop et al. 2017](#); [Michałowski et al. 2017](#); [Smith et al. 2017](#); [Koprowski et al. 2017](#)), contributing at least $\sim 40\%$ of the SFRD through $z \sim 4$. Given the strong correlation between infrared luminosity in galaxies in the local Universe and galaxy mergers, a natural extrapolation to the high-redshift Universe would suggest a strong impact of galaxy mergers on the cosmic star formation rate density. At the same time, the role of mergers in driving the luminosity of heavily star-forming galaxies at high-redshift is under vigorous debate in the community (e.g. [Casey et al. 2009](#); [Dekel et al. 2009b](#); [Davé et al. 2010](#); [Engel et al. 2010](#); [Hayward et al. 2011, 2013b](#); [Narayanan et al. 2010a,b, 2015](#); [Tacconi et al. 2008](#)). Identifying mergers, therefore, is of significant value in understanding their relative role in the growth and evolution of galaxies over cosmic time. Redshifts $z \sim 2-4$ in particular, so-called “Cosmic Noon”, represent an important phase in cosmological galaxy formation where the black hole accretion rate and star formation rate density both peak (see [Shapley 2011](#); [Madau & Dickinson 2014](#), for recent reviews).

There are two primary methods for identifying galaxy mergers: (1) identifying close pairs as galaxies *yet* to merge (e.g. [Barton et al. 2000](#); [Lin et al. 2008](#)), and (2) utilising irregular or disturbed morphologies as an identifier of an *ongoing* or recently elapsed merger (for a recent review see [Conselice 2014](#)).

Within the latter category, there are two broad methods for identifying mergers. The most common approach in using galaxy morphologies to identify ongoing mergers involves visual inspection. In an era of deep HST surveys

alongside massive citizen science campaigns, visual inspection has shown great utility in understanding merger fractions through $z \approx 2$ ([Lintott et al. 2011](#); [Kocevski et al. 2012](#); [Kartaltepe et al. 2015](#)). The second major method, developed principally over the last two decades, involves non-parametric quantitative morphological measures. These have the advantage that they are less subjective and do not require a priori assumptions about morphological characteristic of mergers, but must still be calibrated via visually-identified samples typically at low- z . This paper focuses on studying whether such non-parametric measures are successful at identifying mergers at higher redshifts.

The predominant quantitative galaxy morphology measures utilise the galaxy’s concentration (C), asymmetry (A) and clumpiness (S) (formally known as the CAS system [Conselice 2003](#)), as well as Gini and M_{20} ([Lotz et al. 2004](#)) (to be described quantitatively shortly). More recently, some authors have additionally begun to explore multimode (M), intensity (I) and deviation (D) (MID) statistics ([Freeman et al. 2013](#)). Regions of the parameter space of each set of measures, which were empirically identified using observations of local galaxies, classify morphologies as “normal” or “disturbed” (e.g. [Lotz et al. 2008a](#); [Freeman et al. 2013](#)), where those with “disturbed” morphologies are often considered galaxy mergers. The CAS system tends to identify mostly major mergers while Gini and M_{20} often identify both major and minor mergers ([Conselice 2014](#)). These morphological measures are powerful tools; they have been shown to effectively identify local idealised galaxy mergers ([Lotz et al. 2008a,b](#)), are free of human bias, and scale to large galaxy surveys (e.g. [Cassata et al. 2005](#); [Groggin et al. 2011](#)).

Calibrations of quantitative morphological techniques have been done against low-redshift galaxies, where visual classification of mergers is relatively straight forward. However, at high-redshift, the relative lack of spatial resolution as compared to present-epoch galaxies complicates calibrations. Moreover, galaxies at $z \gtrsim 2$ are generally less organized than their lower-redshift counterparts, with rather complex distributions of gas, dust, and young stars (e.g. [Finlator et al. 2006](#); [Davé et al. 2010](#); [Ivison et al. 2013](#); [Geach et al. 2016](#); [Rujopakarn et al. 2016](#); [Koprowski et al. 2016](#)). It is at present unclear how non-parametric morphological indicators perform in this regime of complex environments in high- z galaxies.

In this regard, numerical simulations of galaxies in evolution provide a promising way forward. By coupling realistic simulations of galaxy evolution with a methodology for creating mock observables, one can calibrate observational techniques against known quantities, and in effect ‘ground-truth’ non-parametric quantitative galaxy morphology indicators.

The method of calibrating quantitative morphology measures via numerical simulations of galaxy evolution was pioneered by [Lotz et al. \(2008a\)](#), who studied the behaviour of morphological measures in idealised simulations of gas-rich major galaxy mergers. By coupling GADGET-3 simulations of galaxy mergers with SUNRISE 3D dust radiative transfer, these authors focused on understanding the dependence of the morphological measures on the observer’s viewing angle, the total mass of the merging galaxies, gas properties, supernova feedback, and the initial orbit of the

merging galaxies. Subsequently, the same group used similar methodologies to study how the morphology measures are affected by the mass ratio between merging galaxies (Lotz et al. 2010a) and the gas fractions of the merging galaxies (Lotz et al. 2010b).

In recent years, the methodology has evolved to utilise bona fide cosmological hydrodynamic simulations of galaxies in evolution. While computationally demanding, cosmological simulations offer the notable advantage of modelling the full cosmic environment of galaxies, and therefore may be advantageous over idealised simulations in studying the characteristically complex environments of high-redshift galaxies.

For example, Torrey et al. (2015), Snyder et al. (2015b) and Bignone et al. (2017) utilised the large-box Illustris cosmological simulation to develop mock catalogs and study galaxy morphologies, with the latter authors focusing specifically on non-parametric morphological indicators. Owing both to particle mass resolution, as well as the computational expense, these authors were unable to employ dust radiative transfer, and instead utilised attenuation calculations in order to generate their mock images. More recent work, therefore, has focused on the cosmological zoom technique in order to better resolve galaxy morphologies at high-redshift; this technique encodes the attractive aspects of both large-scale cosmological simulations and idealised galaxy evolution simulations at the expense of significant computational cost (see Somerville & Davé 2014, for a summary). For example, Snyder et al. (2015a) and Thompson et al. (2015) employed ART and GADGET-3 zoomed in simulations (respectively) of galaxies at $z \gtrsim 1$ to understand quantitative morphological indicators via mock observations. The results have been less conclusive than in the idealised case, with the efficacy of non-parametric statistics in quantifying morphologies and identifying mergers being less clear.

In this paper, we present a systematic study of the non-parametric morphological indicators Gini- M_{20} and CAS of galaxies at redshifts $z \sim 2 - 4$. To do this, we employ high-resolution cosmological zoom galaxy formation simulations that span 2.5 decades in mass, bracketing the mass range that encapsulates proto-Milky Way galaxies through massive submillimetre-luminous systems. These simulations are run with the same star formation feedback modules as the MUFASA cosmological simulations, which have shown to be successful at reproducing a broad range of global galaxy observables (Davé et al. 2016). We couple these simulations to 3D dust radiative transfer simulations in order to model the emergent optical morphologies, and employ image analysis techniques analogous to what is done in observations. The combination of high-resolution zooms using a state-of-the-art galaxy formation model, sophisticated 3D dust radiative transfer, and a careful accounting of instrumental effects makes this study a step forward with respect to previous efforts.

In § 2 we present our galaxy formation simulations. In § 3 we detail our conversion of these simulations to observations, discussing both our radiative transfer calculations, as well as our image analysis techniques. We present our results in § 4, provide discussion in § 5, and conclude in § 6.

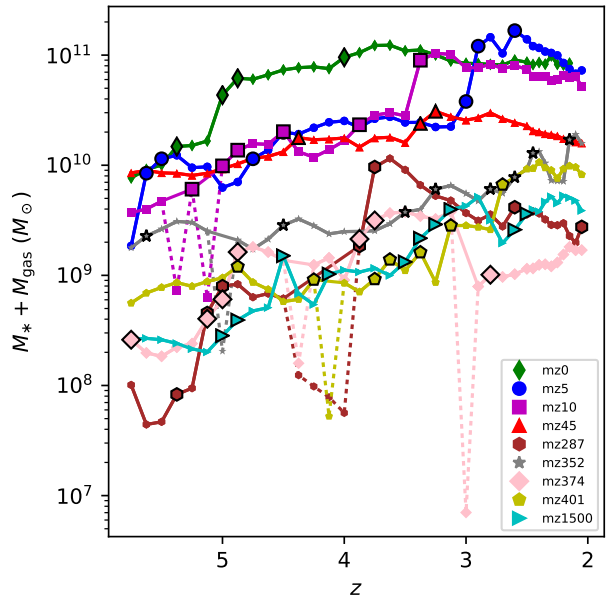


Figure 1. Baryonic mass evolution of the central galaxy from each simulation as a function of redshift. Dashed lines join the baryonic masses of the central galaxy in snapshots that have been omitted from our analysis due to the unphysical baryonic mass drops from previous snapshots. Larger markers with a black outline indicate a baryonic mass increase of at least 25%, from the most recent snapshot connected by a solid line, which corresponds to a major merger. The physical properties of these galaxies are detailed in Table 1.

2 COSMOLOGICAL ZOOM SIMULATIONS

2.1 Simulation Details

To run our galaxy formation simulations, we use a modified version of the hydrodynamic code GIZMO (Hopkins 2015), which draws heavily from the framework of GADGET-3 (Springel 2005). With a cosmology $\Omega_\Lambda = 0.7$, $\Omega_b = 0.048$, $H_0 = 68 \text{ km s}^{-1} \text{ Mpc}^{-1}$ and $\sigma_8 = 0.82$ we generate initial conditions for a $50h^{-1} \text{ Mpc}$ box at $z = 249$ using MUSIC (Hahn & Abel 2011). We run our initial dark matter only simulation, which includes 512^3 particles with a dark matter mass resolution of $7.8 \times 10^8 h^{-1} M_\odot$, down to $z = 0$. At z_{sim} , we use CAESAR¹ (Thompson 2015) to identify halos to re-simulate at a higher resolution. Specifically, we select nine halos to re-simulate at higher resolution. Four of these are selected at $z_{\text{sim}} = 2$, while the latter five are selected at $z_{\text{sim}} = 0$ (though only analysed down to $z = 2$ for the purposes of this paper).

Following the procedure outlined in Hahn & Abel (2011), we set the Lagrangian high-resolution region to be re-simulated for each halo to be the region enclosed by the distance to the farthest dark matter particle included in the dark matter halo at z_{sim} multiplied by a factor of 2.5. We run these zoomed galaxy formation simulations (with baryons) with the same sub-resolution physics employed in the MUFASA cosmological hydrodynamic simulations (Davé et al. 2016, 2017). Like in the MUFASA simulations, we run GIZMO using its meshless finite mass (MFM) method, which

¹ <http://caesar.readthedocs.io/en/latest/>

Table 1. Descriptions of the simulated Galaxies.

Name	Marker Color	Marker Shape	$M_{*,\text{central}}^a$	$M_{*,\text{halo}}^a$	M_{DM}^a	sSFR $_{\text{halo}}^b$	z_{final}
mz0	green	thin diamond	8.4×10^{10}	4.1×10^{11}	4.1×10^{13}	0.0042	2.15
mz5	blue	circle	6.9×10^{10}	8.3×10^{11}	6.3×10^{13}	0.16	2
mz10	magenta	square	6.8×10^{10}	1.6×10^{11}	1.1×10^{13}	0.077	2
mz45	red	down triangle	1.3×10^{10}	1.3×10^{11}	3.7×10^{13}	0.62	2
z0mz287	brown	hexagon	1.0×10^9	2.3×10^9	2.9×10^{11}	0.26	2
z0mz352	grey	star	2.7×10^9	7.2×10^9	9.2×10^{11}	0.84	2
z0mz374	pink	diamond	1.0×10^8	2.9×10^8	1.8×10^{11}	1.4	2
z0mz401	yellow	pentagon	2.4×10^9	3.8×10^9	5.8×10^{11}	1.2	2
z0mz1500	cyan	left triangle	4.5×10^8	7.6×10^8	1.7×10^{11}	1.5	2

^a Masses given in M_{\odot} at $z = z_{\text{final}}$.

^b 50 Myr averaged Specific Star Formation Rate given in Gyr^{-1} at $z = z_{\text{final}}$.

evolves fluid in a way that conserves mass within fluid elements, with a cubic spline kernel with 64 neighbours (Davé et al. 2016). The initial conditions of the MUFASA simulation are the same as those used in our original dark matter simulation.

In the simulations, decoupled two-phase winds are used to model feedback from young stars. The probability of ejection for these winds is given by some fraction, η , of the star formation rate probability. The value of η , which is a best-fit relationship of the mass outflow rate in the Feedback in Realistic Environments (FIRE) simulations (Muratov et al. 2015), is given by

$$\eta = 3.55 \left(\frac{M_*}{10^{10} M_{\odot}} \right)^{-0.351} \quad (1)$$

where the galaxy stellar mass M_* comes from an on-the-fly friends of friends finder (Davé et al. 2016). The velocity of the ejections depends on the galaxy circular velocity using the Muratov et al. (2015) relationship, with an increased amplitude as discussed in Davé et al. (2016). The wind fluid elements remain decoupled until its velocity, relative to surrounding gas, drops below half of the local sound speed. Alternatively, the wind fluid elements will also recouple if either the wind is ejected into gas below a threshold density of 1% of the critical density required for star formation, or if the wind has been decoupled for more than 2% of the Hubble time when it was ejected. See Davé et al. (2016) for a more in-depth discussion of the stellar winds.

Star formation occurs within molecular gas, where the H_2 abundance is given by the prescription detailed in Krumholz et al. (2009), assuming a minimum metallicity of $10^{-3} Z_{\odot}$. We also track the evolution of 11 elements, which consist of H, He, C, N, O, Ne, Mg, Si, S, Ca, and Fe. Specifically, we consider the feedback mechanisms from Type Ia supernovae, Type II supernovae, and Asymptotic Giant Branch stars. See Davé et al. (2016) for specifics about the yields. The only deviation between the physics in our simulations and that of the MUFASA simulations is that we do not include the on-the-fly, heuristic quenching mechanism (Davé et al. 2016).

We run each of the cosmological zoom simulations, with dark matter particle masses of $M_{DM} = 1 \times 10^6 h^{-1} M_{\odot}$ and baryon particle masses of $M_b = 1.9 \times 10^5 h^{-1} M_{\odot}$, down to $z \approx 2^2$. While running the simulations, we used adaptive

gravitational softening (Hopkins 2015); for dark matter, gas, and stars the minimum softening lengths are 280 pc, 7 pc and 2.8 pc, respectively. For each of the simulations, we record 85 snapshots spanning $z \sim 30 - 2$ (except mz0 for which we record 82 snapshots spanning $z \approx 30 - 2.15$), though focus our efforts here on the redshift range $z = 2 - 4$.

2.2 Galaxy Identification

To identify galaxies and halos in each run, we employ CAESAR, which uses a Friends of Friends algorithm with a linking length of 0.2 times the mean inter-particle distance to identify halos and constructs a merger history by linking halos to each other (galaxies are identified using a linking length of $0.2 \times$ the halo linking length). We make use of CAESAR's ability to track galaxies between snapshots and calculate intrinsic properties of the galaxies such as their centres of mass, baryonic masses, etc. For the purposes of our analysis, we identify the central galaxy in a given simulation as the most massive galaxy in the high-resolution halo at the lowest z where it has been simulated.³ See Table 1 for a list of the central galaxies that we follow from each simulation. Figure 1⁴ shows the evolution of the baryonic mass associated with the central galaxy for each simulation over cosmic history, and indicates points in time when we identify a major merger has occurred.

In Figure 2, we show the $M_* - M_{\text{halo}}$ relation for our model halos at integer redshifts $z = 2 - 4$. The shaded curves are the best fit abundance matching models from Behroozi et al. (2013) with an assumed 0.2 dex uncertainty. In Figure 3, we show the SFR- M_* plane of our model galaxies, with the shaded regions showing the best fit main-sequence relations from Speagle et al. (2014) (again, assuming a 0.2 dex uncertainty). Our model galaxies tend to lie on or near the typical SFR- M_* relation, although typically somewhat

run past $z = 2$, though these later time snapshots are not included in this paper, whose focus is galaxies during cosmic noon.

³ Note that there are two galaxies in the high-resolution halo of mz45 of comparable mass. For this analysis, we have identified the central galaxy with slightly higher stellar mass, and slightly smaller baryonic mass as the central galaxy.

⁴ The sizeable dips in baryonic mass shown by dashed lines in Figure 1 owe to a merger temporarily unbinding the majority in the system. Because, during these time frames, the bound systems would be undetectable, we omit these snapshots from our analysis.

² The simulations selected at $z_{\text{sim}} = 0$ were in practice typically

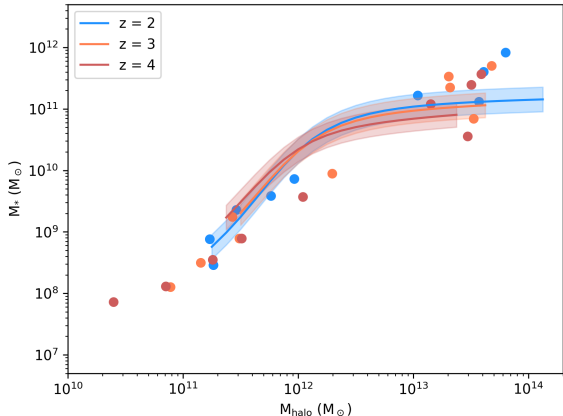


Figure 2. M_* - M_{halo} relation for our model halos at integer redshifts between $z = 2 - 4$. The shaded lines come from the average relations derived by Behroozi et al. (2013), with an assumed 0.2 dex uncertainty.

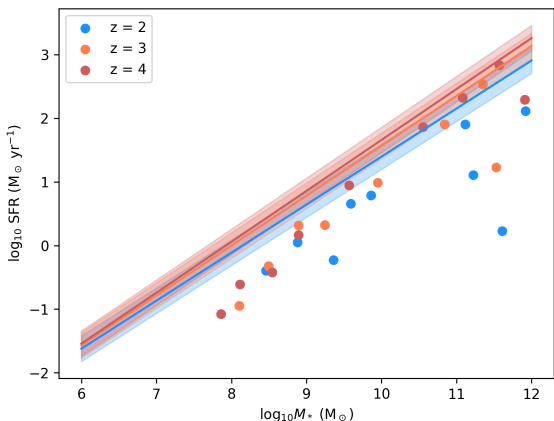


Figure 3. SFR- M_* relation for our model halos at integer redshifts between $z = 2 - 4$. The shaded lines represent the average locations of the star forming main sequence derived by Speagle et al. (2014), with an assumed 0.2 dex uncertainty.

below as has been commonly found for galaxy formation simulations including MUFASA (e.g. Somerville & Davé 2015; Davé et al. 2016). A few galaxies at $z \sim 2$ fall closer to the passive region > 1 dex below the main sequence. These galaxies have exhausted the bulk of their star formation owing to gas consumption and have relatively low gas fractions (see e.g. Feldmann et al. 2016).

Similar to Thompson et al. (2015), we consider a major merger to be at least a 4:1 merger and a minor merger to be at least a 10:1 merger. We use the ratio, R , of the increase in baryonic mass between two snapshots to the baryonic mass of the snapshot before the mass increase to identify galaxy mergers. For each snapshot, we calculate the ratio given by:

$$R = \frac{M_t - M_{(t-1)}}{M_{(t-1)}} \quad (2)$$

where M_t is the baryonic mass of a galaxy at one time and

$M_{(t-1)}$ is the baryonic mass of the central galaxy in the preceding snapshot. Values of R that are ≥ 0.25 or ≥ 0.10 indicate that between the snapshot at t and snapshot at $t-1$, a galaxy that will participate in a major or minor merger has gotten close enough to the central galaxy that the FoF algorithm binds them as a single galaxy.

There are of course some ambiguities in utilising baryonic mass increases as a signature for mergers. First, a rapid succession of minor mergers can mimic a major merger if enough mass is bound to the central galaxy. Similarly, a first passage of a galaxy during a merger followed by a delayed second approach can trigger two merger ‘events’ if the first passage is close enough. Without visual inspection, it is difficult to remove these technical ambiguities. This said, both of these points are somewhat academic; in principle quantitative morphology measures should be blind to these issues.

3 MOCK OBSERVATIONS AND MORPHOLOGICAL MEASURES

3.1 Overview

In this Section, we describe how we generate realistic mock observations of the our model galaxies and how we calculate the quantitative morphology measures from that observation. In Figure 4, we provide a schematic that summarises our methods that is cross-linked with the section number describing those methods quantitatively.

In section (a) Figure 4, the panel labelled ‘‘Stellar Mass Map’’ illustrates the galaxy model that we start with. Although in this panel only the stellar particles assigned to the central galaxy are shown (for simplicity), in reality we perform radiative transfer on all stellar particles in the surrounding region (c.f. § 3.2). The result of radiative transfer is an image like the panel labelled ‘‘RT Output’’ in Figure 4. The specifics of the radiative transfer simulations are detailed in §3.2. We then degrade the radiative transfer output to make it comparable to bona fide observations of galaxies; the produced image resembles the panel labelled ‘‘Observation’’ from Figure 4 and the details of this process are detailed in §3.3. Once we finish degrading the image, we start image analysis which is explained in §3.4.

Section (b) of Figure 4 demonstrates our image analysis techniques, which can be subdivided into several steps. The first of which consists of detecting galaxies in the image; the panel labelled ‘‘Detection Seg. Map’’ shows the regions of the mock observation that are assigned to different galaxies. Although it has been omitted from Figure 4 for space and clarity, we use the stellar mass map to determine which of the detected galaxies corresponds to the central galaxy. Afterwards we ‘‘clean’’ the mock observation by subtracting the noise and masking the light associated with all detected galaxies other than the central galaxy to produce an image like the panel labelled ‘‘Cleaned.’’

At this point, we move onto the task of calculating asymmetry (A) and concentration (C). To do this we calculate the Petrosian radius (r_p) and find the centre of the galaxy such that the region enclosed within $1.5r_p$ has minimized A . We recalculate r_p and again search for the centre at which A is minimized using the new r_p . The panel titled ‘‘ r_p ’’

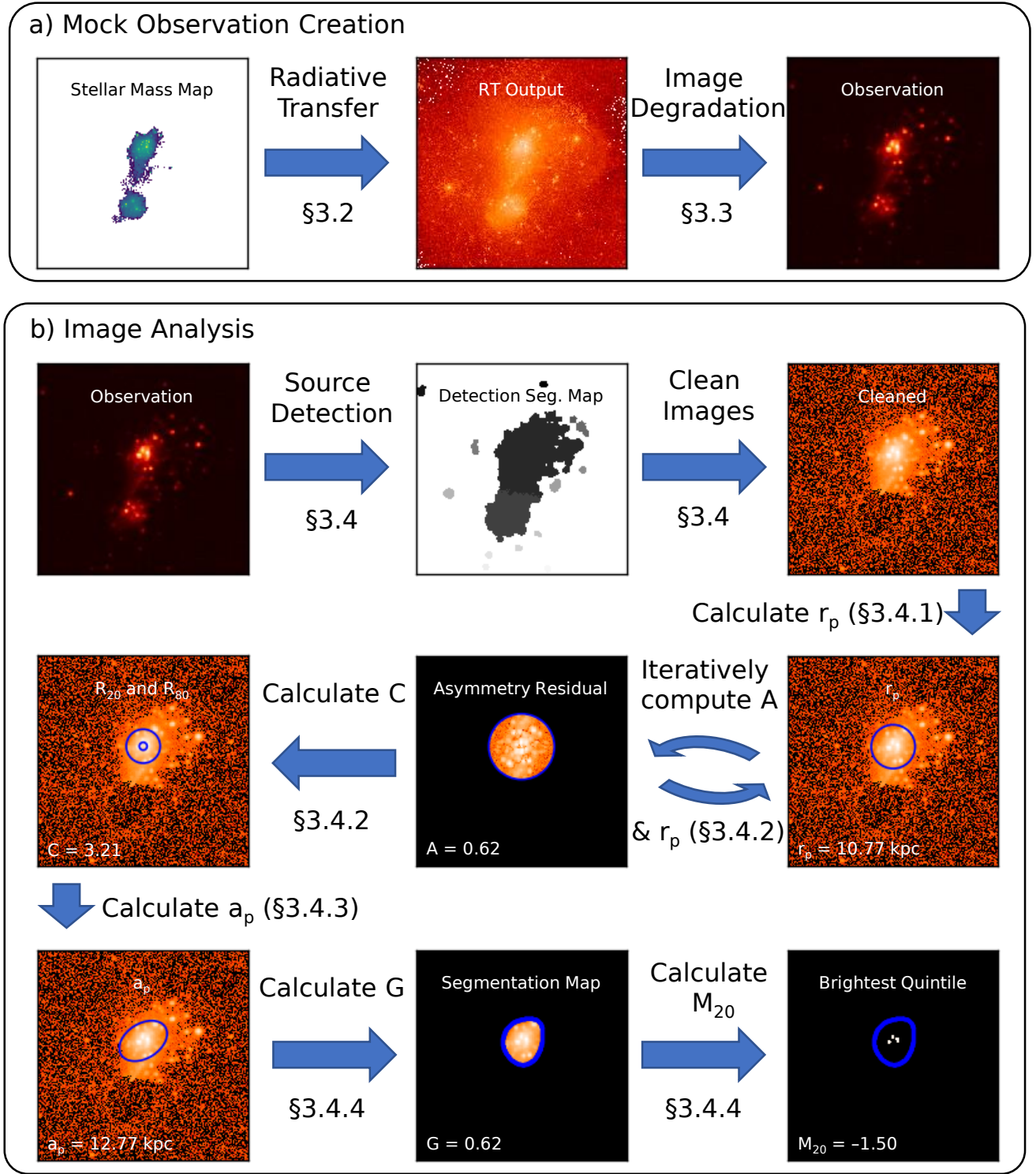


Figure 4. Illustration of the steps involved with the creation of a mock observation (section a)) and the analysis of the observation (section b)) for a single line of sight of the central galaxy of *mz10* at $z \approx 2.8$. The panel labelled “Stellar Mass Map” shows the projection of all of the stellar mass particles assigned by CAESAR to the central galaxy and represents the galaxy model we start with. The panel titled “RT Output” shows the image produced by POWDERDAY and the mock observation created by degrading the initial image is shown in the panels titled “Observation”. The panel labelled “Detection Seg. Map” illustrates all of the detected galaxies in the image. “Cleaned Image” illustrates the observation after masking and sky-subtraction while “ r_p ” shows the same image with the Petrosian radius overplotted. The panel called “Asymmetry Residuals” shows the absolute values of the residuals used to measure A . The panel labelled “ r_{20} and r_{80} ” shows the radii used to compute C whereas the panel labelled “ a_p ” illustrates an ellipse with the ellipticity and position angle of the best-fit ellipse and the Petrosian semi-majors. The outline of the segmentation map used to calculate $G - M_{20}$ is shown in “Segmentation Map” and “Brightest Quintile.” In the former, the contents of the segmentation map is shown while in the latter, only the brightest quintile is shown.

illustrates the size of the final calculated r_p while the panel titled “Asymmetry Residual” shows the absolute value of the difference of the region used to calculate A and the region rotated by 180° . We calculate the radii that enclose 20 per cent and 80 per cent of the galaxy’s light in order to determine C . These radii are shown in the panel labelled “ r_{20} and r_{80} ”. The final stage of image analysis is made up of the calculation of the Petrosian semi-major axis (a_p), Gini (G) and M_{20} . We calculate a_p at the centre where A was minimized; it is illustrated in the panel called “ a_p .” The panels from figure 4 named “Segmentation Map” and “Brightest Quintile” show intermediary results critical to the calculation of G and M_{20} .

In what follows, we describe these methods in greater detail. This said, the reader principally interested in the main results may skip the remainder of this section without loss of continuity. Finally, we note that in the Appendices § A and § B, we validate our methods against test simulation data sets from the literature.

3.2 Radiative Transfer Simulation

We employ the POWDERDAY dust radiative transfer software (Narayanan et al. 2015, 2017), which is built on YT (Turk et al. 2011), HYPERION (Robitaille 2011), and FSPS (Conroy & Gunn 2010) in order to generate raw mock images of the galaxies from the GIZMO simulations. In short, POWDERDAY generates stellar SEDs from the stars formed in the cosmological simulations, and propagates these through the dusty interstellar medium (ISM) in a Monte Carlo and iterative fashion until the radiation field and dust temperatures are converged.

The stellar SEDs are calculated as simple stellar populations generated in FSPS⁵, with the ages and metallicities taken directly from the galaxy formation simulation. We assume a Kroupa (2002) stellar initial mass function, and the Padova isochrones (Marigo & Girardi 2007; Marigo et al. 2008). We calculate the attenuation these stars see via HYPERION dust radiative transfer. We construct an octree grid from the hydrodynamic simulation upon which to perform the radiative transfer by projecting the metal mass using a spline smoothing kernel. The octree is constructed by placing the entire simulated region onto a grid with a single cell, and then recursively refining until a maximum number of gas particles (here, 64) are contained within a cell. Functionally, the octree is constructed within YT (Turk et al. 2011).

The radiative transfer is propagated via a Monte Carlo method (Robitaille 2011), and the radiative equilibrium calculation uses the Lucy (1999) algorithm. We determine convergence when the dust temperature in 99% of the cells has changed by less than 1% between iterations. We assume a $R_v = 3.15$ Weingartner & Draine (2001) dust size distribution. The dust mass is assumed to be 40% of the projected metal mass, following constraints from both local and high- z galaxies (Dwek 1998; Vladilo 1998; Watson 2011).

We centre the observations on the most massive progenitors of the most massive galaxy in the simulation at

Table 2. Values of the essential parameters for the SEP Background class and extract function and the equivalent SEXTRACTOR parameters. The SEP parameters that lack an equivalent SEXTRACTOR parameter have been omitted from the table.

SEP param	SEXTRACTOR param	value
bw, bh	BACK_FILTERSIZE	128, 128
fw, fh	BACK_SIZE	1, 1
minarea	DETECT_MINAREA	50
deblend_nthresh	DEBLEND_NTHRESH	16
deblend_cont	DEBLEND_MINCONT	0.05
clean	CLEAN	True
clean_param	CLEAN_PARAM	1.0

$z = 2$ and image 23 snapshots from $z = 2$ to $z = 4$. Individual images made in 16 cameras oriented with respect to the simulation axes. The cameras each view the centre of mass of the central galaxy and are positioned at all combinations of θ and ϕ , within the sets $\theta \in [0^\circ, 30^\circ, 60^\circ, 90^\circ]$ and $\phi \in [0^\circ, 30^\circ, 60^\circ, 90^\circ]$. The images are produced at $\lambda_{\text{obs}} = 4325 \text{ \AA}$ to simulate an observation in the rest-frame B filter. Our final model images are 512×512 pixels.

The physical size of the imaged region is dependent on the angular diameter distance at for the z of the snapshot is chosen such that the resulting image has a pixel scale of $\sim 0.05'' \text{ pix}^{-1}$, comparable to that of *HST*’s Wide Field Camera 3 (WFC3). The brightness of the image is finally scaled to the luminosity distance at the redshift of the snapshot.

3.3 Image Degradation

To best compare our model images to observations, we roughly follow the procedures employed by Lotz et al. (2008a) and Snyder et al. (2015b) to degrade the images produced by the radiative transfer simulations. We convolve the image with a Gaussian beam with full width at half maximum (FWHM) corresponding to the Rayleigh criterion appropriate for the *HST* mirror size. We then add sky noise targeting an average signal to noise ratio, $\langle SNR \rangle$, of at least 20 to minimize the effects of $\langle SNR \rangle$ on our analysis. We do this by adding random Poisson noise such that the $\langle SNR \rangle$ of the central galaxy’s pixels is 25. We determine the central galaxy’s pixels by identifying the non-zero pixels when the galaxy’s stellar mass is projected onto an array of equal resolution to the image. We deliberately aim for adding noise such that the galaxy’s pixels have an $\langle SNR \rangle$ of 25, to increase the number of galaxies with $\langle SNR \rangle \geq 20$ because we expect the central galaxy’s light to be slightly smeared out relative to the pixels where it has non-zero projected stellar mass. Thus when a central galaxy is detected from the observation, it may include additional pixels not included in its projected stellar mass, which may cause it to have an $\langle SNR \rangle$ below 25.

3.4 Image Analysis

We make use of the python library, SEP (Barbary 2016), to detect sources in the mock images and generate initial segmentation maps. This library applies many of the algorithms from SEXTRACTOR (Bertin & Arnouts 1996), on

⁵ Functionally, we use the python FSPS hooks located at <https://github.com/dfm/python-fsps>

images stored in memory. See Table 2 for a list of parameters used for SEP that have equivalent parameters in SEXTRACTOR. We make a temporary sky subtracted image and detect sources with the detection threshold set to the global background RMS of the background and use the applicable parameters listed in Table 2. While performing extraction, we use the filter distributed with SEXTRACTOR in “tophat_5.0_5x5.conv” (Bertin & Arnouts 1996) and set the filter_type parameter to “conv.” We then identify the central galaxy in the image, using the projection of the central galaxy’s stellar mass map that we computed when adding noise. We sum the stellar mass enclosed in the regions assigned to each detected galaxies in the initial detection segmentation map produced by SEP. The region enclosing the greatest projected stellar mass is identified as the detection of the central galaxy. We generate a masked image by copying the original mock observation and setting the pixels enclosed by the initial segmentation maps of all galaxies other than the central galaxy equal to the noise value we previously added to the pixels.

Unless otherwise stated, from this point on we follow the algorithm employed in the code used in Lotz et al. (2008a). Our next step is to identify the largest square region of the masked image that is no bigger than 50x50 pixels, is no smaller than 12x12 pixels, does not overlap with any of the detected galaxies and contains more than 90 per cent non-zero pixels. Then, we generate a sky-subtracted image by subtracting the average flux the square region from the masked image. At this point, we move onto computing the central galaxy’s Petrosian radius (r_p), and semi-major axis (a_p), concentration (C) and asymmetry (A) of the CAS statistics (Conselice 2003), and Gini and M_{20} (Lotz et al. 2004). Rather than following the algorithms employed by Lotz et al. (2008a) to calculate the centre of the galaxy and the parameters for the best-fit ellipse, we use the values calculated by SEP.

3.4.1 Petrosian Radius

We adopt the same definition for the Petrosian radius (r_p) as described by Lotz et al. (2004). The Petrosian radius is defined as the radius at which the quotient of the the surface brightness enclosed by a circular annulus, $\mu(r_p)$, and the mean surface brightness enclosed by a circular aperture, $\bar{\mu}(r < r_p)$, is equal to a constant, η , or

$$\eta = \frac{\mu(r_p)}{\bar{\mu}(r < r_p)} \quad (3)$$

By convention, $\eta = 0.2$. To compute the size of apertures, we use the IDL task dist_ellipse from the IDL Astronomy Library (ASTROLIB)⁶ (Landsman 1993) with elliptical parameters corresponding to a circle to determine the pixels that belong to different apertures. We then employ an iterative algorithm that iterates over the radius, r , of the circular aperture and calculates η for each aperture. The algorithm starts with $r = 2$ pixels and between iteration r is increased by 1. The algorithm terminates when $\eta \geq 0.2$ and we determine r_p using $r_p = r(0.8 + \eta)$.

⁶ <https://idlastro.gsfc.nasa.gov/homepage.html>

3.4.2 Asymmetry and Concentration

The asymmetry (A) of a galaxy quantifies the rotational symmetry of a galaxy’s light (Conselice 2003). To determine A , the image of a galaxy is rotated by 180° about its centre and is subtracted from the original image. The absolute value of the residuals summed and divided by the sum of the fluxes in the original image and the average asymmetry of the background is subtracted:

$$A = \frac{\sum |I_0 - I_{180}|}{\sum I_0} - B_{180}. \quad (4)$$

Here, I_0 and I_{180} represent the flux values of individual pixels in the original image and rotated images, respectively, while B_{180} is the average background asymmetry. The summations only sum over pixels within $1.5r_p$ of the galaxy’s centre which is chosen such that A is minimized.

To compute A at a particular centre, we rotate the image about the centre using bilinear interpolation and subtract the rotated image from the original image. We use the algorithm from dist_ellipse (Landsman 1993) to identify all pixels that lie within $1.5r_p$ of the galaxy’s centre. Next, we sum the absolute value of the residuals that lie within those pixels and divide by the sum of the absolute value of the original fluxes at those pixels. At this point, we have computed the uncorrected asymmetry and all that remains is to compute the average background asymmetry, B_{180} . We take the square background region of the sky-subtracted image, which include the same pixels from the square background region we identified to perform sky-subtraction, rotate the region about its centre, subtract the rotated values from the original values, sum the absolute value of the residuals and divide by the number of pixels in the region. Then, we multiply the quotient by the number of pixels that lie within $1.5r_p$ of the galaxy’s centre and divide by the sum of the absolute value of the galaxy’s fluxes at those pixels, which gives B_{180} . Subtracting B_{180} from the uncorrected asymmetry, gives the value of A at that centre.

In practice, we start trying to calculate the A using the r_p calculated when the centre of the galaxy was set to be the centre of the best-fit ellipse. We then minimize Equation 4 using modified Powell’s method, which determines the centre at which A is minimized starting from the centre of the best-fit ellipse. The result is the initial guess for A , and the initial guess for the centre. Then, we recalculate r_p at this new centre, and again use the modified Powell’s method to minimize A using the r_p and the new centre as a guess. As a result, we determine the galaxy’s A and the centre where A is minimized.

We use the definition of Concentration (C) given by Bershadsky et al. (2000). It is the ratio of the radii at which circular apertures contain 20 and 80 per cent of a galaxy’s total flux:

$$C = 5 \log_{10} \left(\frac{r_{80}}{r_{20}} \right). \quad (5)$$

Like Conselice (2003), we consider the total flux to be the flux contained in $1.5r_p$. The galaxy’s centre used in the calculation of C is the centre determined while measuring A . When computing C , we start by recalculating r_p at the centre where A is minimized. Next, we use a similar iterative method to tabulate the fraction of the flux enclosed within an aperture of radius $1.5r_p$ for all apertures with positive in-

teger radii less than $1.5r_p$. Then, we use linear interpolation to determine the smallest radii to contain 0.2 and 0.8 of the total flux, which yields r_{20} and r_{80} . Finally, we determine C with Equation 5.

3.4.3 Petrosian semi-major axis

After computing the Concentration C , we then calculate the Petrosian semi-major axis (a_p), or the elliptical Petrosian radius, (Lotz et al. 2004), which is defined in the same way as r_p except that elliptical apertures and annuli are used. To calculate it, we use an algorithm that differs from the one employed by Lotz et al. (2008a) and draws significant inspiration from the algorithm employed in the photometric pipeline of the Sloan Digital Sky Survey (SDSS) to compute r_p (Strauss et al. 2002). Let θ be the angular distance between the centre of an object and the edge of an annulus or aperture. Following Strauss et al. (2002), we can rewrite Equation 3, the equation for the Petrosian ratio, as

$$\eta(\theta) = \frac{\int_{r_{in}\theta}^{r_{out}\theta} I(\theta') dA / [A(r_{out}\theta) - A(r_{in}\theta)]}{\int_0^\theta I(\theta') dA / A(\theta)}. \quad (6)$$

In the above equation r_{in} and r_{out} are constants that represent the inner and outer limits of an annulus. Additionally, $A(\theta)$ and $I(\theta)$ are the area and average flux enclosed by an elliptical aperture with a semi-major axis θ . For a given galaxy, all apertures have a constant ellipticity, $ell = 1 - b/a$. Like with r_p , the Petrosian semi-major axis, a_p , is defined as the value of θ at which $\eta = 0.2$.

Suppose $L(\theta)$ is the function describing the cumulative light profile of a galaxy. It gives the total light enclosed within a semi-major axis θ and is defined as

$$L(\theta) = \int_0^\theta I(\theta') dA. \quad (7)$$

We can substitute Equation 7 into Equation 6 to get

$$\eta(\theta) = \frac{[L(r_{out}\theta) - L(r_{in}\theta)] / [A(r_{out}\theta) - A(r_{in}\theta)]}{L(\theta) / A(\theta)}. \quad (8)$$

Because all of our apertures have fixed ellipticity, we know that $A(\theta) = \pi\theta^2(1 - ell)$. Using this to simplify our equation for η , we find

$$\eta(\theta) = \frac{L(r_{out}\theta) - L(r_{in}\theta)}{L(\theta)(r_{out}^2 - r_{in}^2)}. \quad (9)$$

Finally, a_p can be found by just solving this equation for when $\eta = 0.2$.

To actually calculate a_p , we start by determining points along the cumulative light profile of the galaxy, $L(\theta_i)$, for 56 exponentially spaced semi-major axes θ_i . The minimum semi-major axis, θ_0 is the semi-major of an ellipse that encloses an area of 1 pix^2 and the values of the remaining semi-major axes are given by $\theta_i = (1.057/0.9457)\theta_{i-1}$. After we compute the semi-major axes, we compute the flux enclosed within the elliptical aperture with a semi-major axis of θ_0 and the fluxes enclosed in elliptical apertures extending from θ_{i-1} to θ_i for the remaining semi-major axis. We will refer to these flux measurements as $F(\theta_i)$. The elliptical aperture and elliptical annuli each have ellipticity equal to that of the best-fit ellipse and are all centred on the centre of the galaxy where A had been minimized. To perform the actual photometry we use the `sum_ellipse` and `sum_functions`

from the python package, `SEP` (Barbary 2016) and we have the functions calculate the exact overlap between the pixels and the apertures. After computing $F(\theta_i)$, we calculate $L(\theta_i)$ using $L(\theta_i) = \sum_{k=0}^{i-1} F(\theta_k)$.

Like the SDSS photometric pipeline, we construct a cubic spline with the “not-a-knot” condition to find $\text{asinh}(L)$ as a function $\text{asinh}(\theta)$ (Strauss et al. 2002). To construct the spline, we use all values of θ_i and $L(\theta_i)$, and set $L(0) = 0$. Similar to the SDSS photometric pipeline, we take asinh of all of our θ_i and $L(\theta_i)$ because of the large dynamic range in $L(\theta)$ and because $\text{asinh}x$ is better behaved than $\log x$ when x approaches 0 (Strauss et al. 2002). We use Equation 9, our cubic spline, $r_{in} = 0.84$, and $r_{out} = 1.19$ to determine $\eta(\theta_i)$. Then, we use another “not-a-knot” cubic spline to find η as a function of $\text{asinh}(\theta)$. Finally, a_p is given by the value of θ for which $\eta = 0.2$. If there are multiple values of a_p , we choose the smallest value of that is ≥ 5 pix , if applicable; however if all values are smaller than 5 pix , choose the maximum value. Like in the algorithm employed by Lotz et al. (2008a), if $a_p < 2$ pix , we set a_p equal to the value of r_p .

There are additional differences from the algorithm employed in the SDSS photometric pipeline beyond our change to make the algorithm apply to a_p . These changes include calculating points of the cumulative light profile $L(\theta_i)$ at more θ_i values that were more closely spaced, not using the “taut” condition for our cubic splines, setting $L(0) = 0$, and using different values of r_{in} and r_{out} (Strauss et al. 2002). See Appendix E for an in-depth explanation as to why we employ this algorithm to compute a_p instead of that which was employed by Lotz et al. (2008a).

3.4.4 Gini and M_{20}

The Gini coefficient (G) describes the distribution of light among a pixels in a galaxy’s segmentation map constructed with procedure described by Lotz et al. (2004). Specifically, the value of G is given by

$$G = \frac{1}{|\bar{f}|n(n-1)} \sum_i^n (2i - n - 1) |f_i| \quad (10)$$

where n is the number of pixels that are in the object’s segmentation map, $|f_i|$ is the i th smallest absolute flux value in the segmentation map, and $|\bar{f}| = \sum_i^n \frac{|f_i|}{n}$. Higher values of G indicate that the light is less equitably distributed among a galaxy’s pixels while lower values of G indicate that the light is more equitably distributed among a galaxy’s pixels (Lotz et al. 2008a). A value of 0 means that all pixels have the same brightness while a value of 1 means that all of the light comes from a single pixel (Lotz et al. 2004).

Before calculating G , we first determine the segmentation map using a_p . To determine the segmentation map at a given centre we first convolve the image with a Gaussian of $\sigma = a_p/5$ to get the smoothed image which is only used for determining the segmentation map. Following the algorithm used by Lotz et al. (2008a), we set the FWHM of the Gaussian kernel to the maximum of $a_p/10$, 3 times the FWHM used for the point spread function, and 1.0. We also set the width of the kernel to 5 times the FWHM of the kernel, rounded down to the nearest integer. Next, we identify pixels in the smoothed image with at least as bright as the average surface brightness μ at a_p in the smoothed

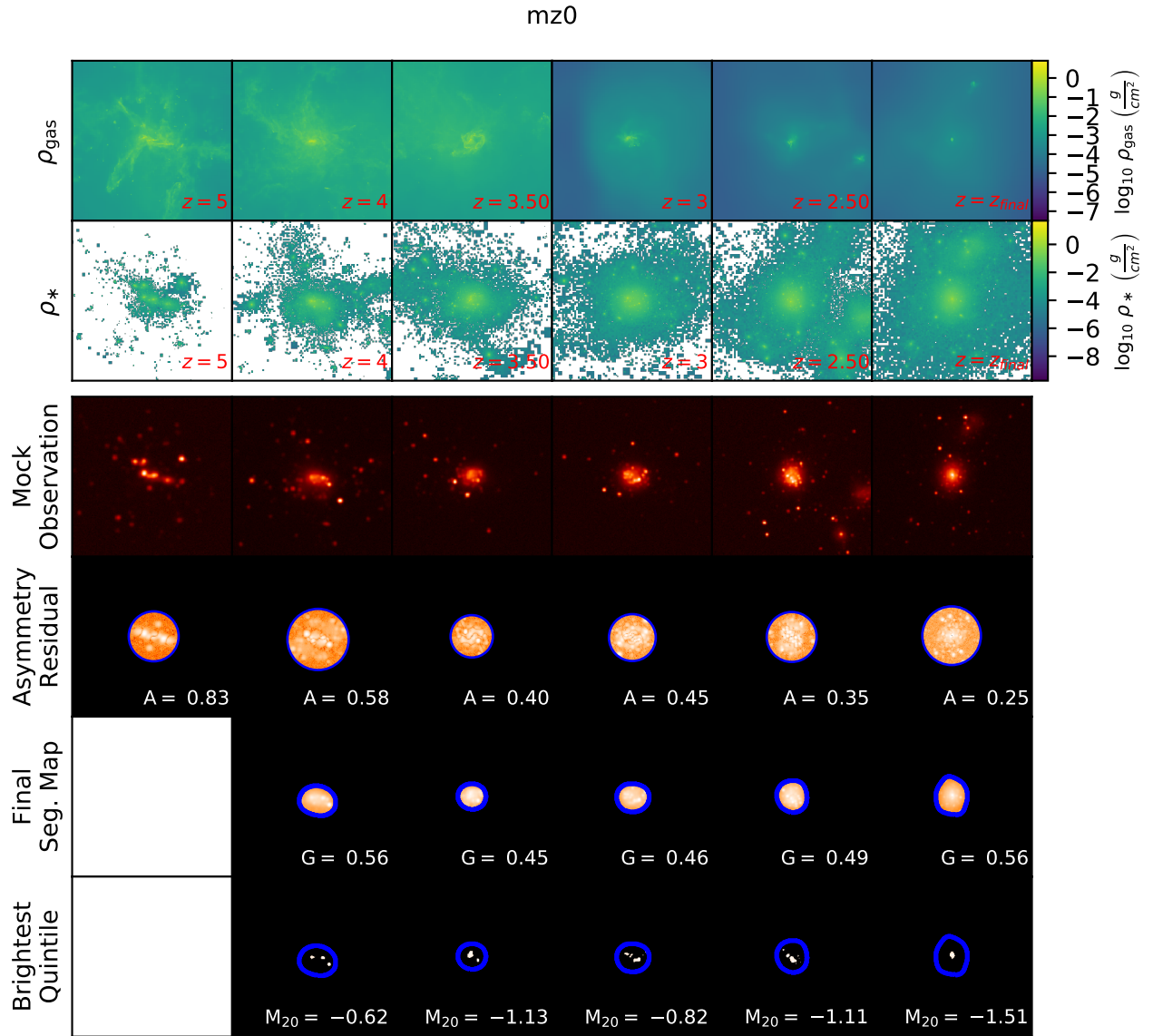


Figure 5. Gas surface density, stellar surface density, mock B -band observations, asymmetry residuals, final segmentation maps, and brightest quintile centred on the centre of mass of the central galaxy of mz0, generated along a single line of sight, at $z \approx 5, 4, 3.5, 3, 2.5$ and z_{final} . All gas surface density plots share a single colourmap, as do the stellar surface density plots. Each panels has an angular size of $\approx 12.8''$. The final segmentation map and brightest quintile has been omitted at the z when the final segmentation map has $(\text{SNR}) < 20$ or is not contiguous.

image. To measure $\mu(a_p)$, we take the average of all pixels in the smoothed image we determine to lie between $a_p - 1$ and $a_p + 1$ using the algorithm from the IDL task `dist_ellipse` (Landsman 1993). Then, we determine all pixels at least as bright as $\mu(a_p)$. If there are less than 2 pixels brighter than μ , we cut μ in half, and repeat this process of dividing μ in half until we have at least 2 pixels.

At this point, we generate an array where all pixels in the segmentation map have values of 10 and all other pixels have values of 0, and apply the algorithm employed in the IDL task `sigma_filter` from `ASTROLIB`. All pixels in the resulting array with non-zero values are identified as pixels in the segmentation map. This procedure removes completely isolated bright pixels from the segmentation map segmenta-

tion map and includes dimmer pixels that are predominantly surrounded by pixels in the segmentation map.

We calculate the segmentation map at the centre where the total second order moment, M_{tot} , is minimized. The total second order moment at a given centre, (x_c, y_c) , is given by

$$M_{\text{tot}} = \sum_i^n M_i = \sum_i^n f_i [(x_i - x_c)^2 + (y_i - y_c)^2] \quad (11)$$

where f_i is the flux of the pixel at (x_i, y_i) . This formula only applies to pixels in the segmentation map centred at (x_c, y_c) . To determine the centre at which M_{tot} is minimized we use the modified Powell's method on a function that computes the segmentation map and M_{tot} at various centres. We supply the centre at which A is minimized as an initial guess.

Once we have the segmentation map where M_{tot} is minimized, we check to see if all pixels in the segmentation map are contiguous. If so, we compute G using Equation 10. Otherwise we simply do not calculate G or M_{20} for that galaxy.

Additionally, we calculate M_{20} , the normalized second-order moment of the brightest 20% of a galaxy's light, from the same segmentation map used to calculate G . We determine M_{20} by summing M_i for the pixels ordered by decreasing flux until the total flux of the pixels is 20% of the total flux in the segmentation map, and normalizing the sum by M_{tot} . This is summarized by

$$M_{20} = \log_{10} \left(\frac{\sum_i^n M_i}{M_{tot}} \right), \text{ while } \sum_i f_i < 0.2 f_{tot}. \quad (12)$$

where f_{tot} is the total flux in the segmentation map. According to Lotz et al. (2008a) find that more positive values ($M_{20} \geq -1$), intermediate values ($M_{20} \sim -1$), and more negative values ($M_{20} \leq -2$) typically indicate mergers, late type galaxies, and early type galaxies, respectively. We calculate M_{20} by applying Equation 12 to the segmentation map used to calculate G .

After we calculate M_{20} , we determine the average signal-to-noise ratio per pixel, $\langle SNR \rangle$, for the segmentation map of the galaxy. Following Lotz et al. (2004), we compute $\langle SNR \rangle$ via:

$$\langle SNR \rangle = \frac{1}{n} \sum_i^n \frac{f_i}{\sqrt{\sigma_{sky}^2 + f_i}}, \quad (13)$$

where n is the number of pixels in the segmentation map, f_i is the flux of the i th pixel in the segmentation map, and σ_{sky} is the sky noise. To determine σ_{sky} , we apply a transposed version of the IDL task `robust_sigma` from `ASTROLIB` (Landsman 1993) on the square region of the sky subtracted image that we use to compute B_{180} in the calculation of A .

4 MORPHOLOGY ANALYSIS

4.1 Model Sample Selection

We now turn to analysis of the evolution of morphology over $z \sim 2 - 4$. We examine morphological parameters along 13 lines of sight⁷, and consider galaxies which were computed with contiguous segmentation maps that have $\langle SNR \rangle \geq 20$. We also manually inspect segmentation maps and discard 5 additional individual sightlines (out of all sightlines and all snapshots) in which the segmentation maps enclose the majority of the image, and are obviously incorrectly computed; these predominantly come from the lowest mass model.

For our CAS analysis, we manually inspect images produced for all observed galaxies, similar to the panel labelled ‘‘Cleaned’’ in Figure 4 and discard values for galaxies when the circles are very obviously offset from the central galaxy.

⁷ While the galaxies are all imaged by 16 cameras in `POWDERDAY`, the cameras positioned at $(\theta, \phi) = (0^\circ, 0^\circ), (0^\circ, 30^\circ), (0^\circ, 60^\circ),$ and $(0^\circ, 90^\circ)$ all look along the same line of sight. The only difference in the images produced by these cameras is that they are rotated in the plane of the sky, and are therefore not unique. Thus of those 4 cameras, we only consider the morphological parameters measured with the camera at $(0^\circ, 0^\circ)$.

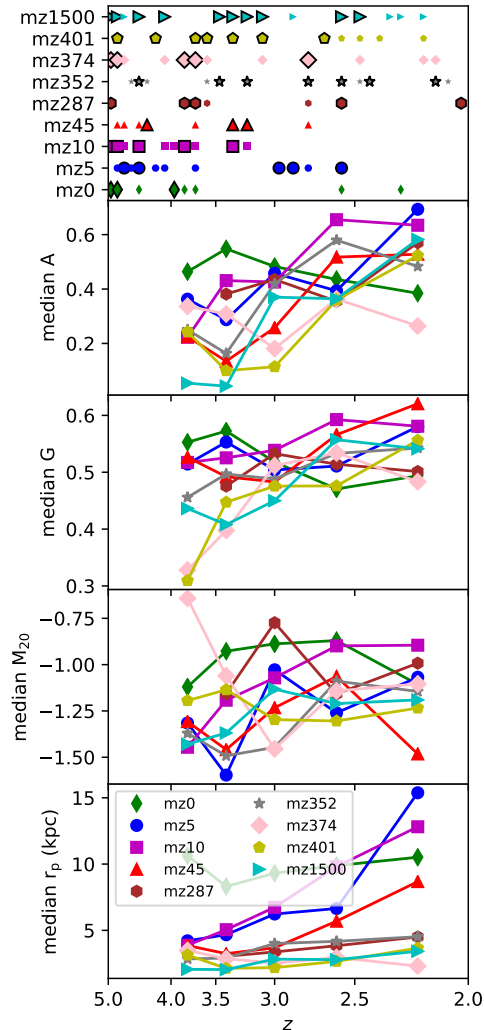


Figure 6. Galaxy merger history and evolution of A , G , M_{20} and the Petrosian Radius r_P as functions of z . The top panel illustrates mass increases indicative of galaxy merger; larger markers with black outline correspond to mass increases indicative of major mergers ($R \geq 0.25$), whereas smaller markers without outlines indicate mass increases indicative of minor mergers ($0.10 \leq R < 0.25$). In the panels showing the evolution of the morphology measures we only show the region between $z = 2 - 4$ as non-contiguous segmentation maps and low SNR at higher redshifts make the model data somewhat incomplete.

In doing this, we cut measurements for one sightline from $mz5$, two sightlines from $mz10$, one sightline from $mz45$, two sightlines from $mz287$, one sightline from $mz374$, two sightlines from $mz401$ and three sightlines from $mz1500$.

After imposing these two sets of filtering criteria, we have $G - M_{20}$ data for 1747 valid sightlines from all of our galaxy snapshots, and 2631 measurements of $C - A$ data from all of our galaxy snapshots.

4.2 Evolution of Non-Parametric Morphology Parameters

In Figure 5 we illustrate the evolution of the gas and stellar morphology of model *mz0* at important redshift intervals. We additionally show the mock *B* band (4325 Å) observation, the asymmetry residual, final segmentation map, and brightest quintile measurement. These latter three quantities are important for calculating *A*, *G* and M_{20} , respectively. In Appendix C, we show a similar series of postage stamps for all zoom simulations in our simulation suite⁸.

Figure 5 and Figures C1-C8 reveal a number of salient points. First, the morphologies of high-redshift galaxies are highly complex compared to local galaxies. The rich accretion histories of satellite galaxies result in complex environments with extended morphologies, multiple nuclei, and stellar bridges at nearly all redshifts. For all galaxies, the morphologies become more extended at later times ($z \sim 2$) as more subhalos accrete over cosmic time.

Second, higher mass galaxies tend to have more complex and spatially distributed optical emission than lower mass systems. The massive systems have extended optical morphologies from early times ($z \sim 5$). Accordingly, aside from the most massive halo in our model sample (*mz0*, which we will discuss shortly), this results in elevated *G* and *A* measures as multiple nuclei and distorted morphologies are ubiquitous over the redshift range considered for the most massive galaxies.

Third, for the lowest mass galaxies in our simulation sample, the contribution of satellites to the optical flux at very high ($z \sim 5$) redshifts is insufficient enough that the optical morphologies remain compact until later times ($z \sim 2$). Because the regions used to compute the non-parametric measures $G - M_{20}$ and *A* are so compact, they are highly sensitive to small irregularities in the optical morphology (e.g. if the nucleus is slightly elongated or slightly offset from the centre of the envelope). At mid to later times ($z \sim 3 - 2$), the low mass galaxies each undergo a series of mergers in quick succession. Due to the short intervals of time between mergers ($\lesssim 0.55$ Gyr), the galaxies are unable to relax, making it easier for non-parametric measures to register ongoing mergers.

These trends are quantitatively apparent in Figure 6, where we present the evolution with redshift of non-parametric morphology measures for our model galaxies. The lowest mass galaxies have the lowest *G*, *A*, and M_{20} values at early times, due to the difficulty of detecting infalling satellites. As the central galaxies grow, mergers impact *G* and M_{20} more and these values tend to rise toward later times. More massive galaxies (e.g. models *mz5*, *mz10*) have relatively elevated non-parametric morphology measures throughout the redshift range being considered, though the most massive halo in our model sample (*mz0*) deviates from this trend. The elevated *G*, *A* and M_{20} values for these massive galaxies (*mz5*, *mz10*) lie in the classical merger range of these non-parametric indicators, even at times well-separated from major mergers due to a rich accretion history of subhalos.

⁸ We note that we reject images that have either poor SNR or non-contiguous segmentation maps, and so the redshift stamps are similar, though not identical from model to model.

This said, while there are broad trends with galaxy/halo mass, it important to recognise that the diversity in halo accretion history can cause dispersion or slight deviations in these trends. To see this, we examine the specific cases of low mass galaxy *mz287* and the most massive system in our sample, *mz0*. As a reminder, *mz287* is a proto-Milky Way mass galaxy, while *mz0* has a mass comparable to the most massive galaxies detected at $z \sim 2$.

At early times, low mass galaxy *mz287* differs from these trends with its elevated *A*, *G*, and M_{20} , that are mostly indicative of mergers. For comparison intermediate mass galaxies and other low mass galaxies all have far lower *A*, *G*, and M_{20} . The elevated *A*, *G*, and M_{20} can be partially explained by the abundance of satellites and how it takes on a relatively extended morphology during these early mergers. Although low mass galaxy *mz374* and intermediate galaxy *mz401* also are surrounded by several satellites at $z \lesssim 4$, in comparison to *mz287* their interactions with satellites are much shorter, and they quickly relax following each merger not becoming as extended.

The most massive galaxy in our simulation suite, model *mz0* also deviates slightly from these broad trends in a subtle way. This galaxy exhibits somewhat elevated *G*, *A* and M_{20} values early on (as expected given its mass), though these values plateau, or even decrease at later times. This is in contrast to almost all other model halos which have rising *G*, *A*, M_{20} values with time. The origin of this trend is subtle. The rapid accretion history at early times gives rise to significant amounts of extended light that has a relatively uniform distribution within the final segmentation map. The spatial uniformity drives down *G* and *A* values, even during periods of heavy bombardment. Whether or not model *mz0* is representative of all galaxies at this extreme end of the mass function (i.e. that represented, likely, by high- z dusty star forming galaxies) is unclear. More simulations in this mass regime will be revealing, and are deferred to future work.

4.3 $G - M_{20}$ and $C - A$ Space

After having built our intuition in § 4.2, we now consider our model galaxies in $G - M_{20}$ and $C - A$ space. In Figure 7, we present the location of our model galaxies in $G - M_{20}$ space, and in Figure 8, we show the same in $C - A$ space. In the top row of each, we show all of our model galaxies in three redshift bins, and in the subsequent rows, we bin the galaxies by mass in $G - M_{20}$ and $C - A$ space. We additionally label the plot with the traditional Hubble morphological classification associated with particular regions in these plots (Lotz et al. 2008b; Conselice 2003). The points shown are sightline medians. The generic trends discussed in § 4.2 become more apparent in $G - M_{20}$ and $C - A$ space.

On average, galaxies move from the non-merger region of $G - M_{20}$ and $C - A$ space to the merger region as they evolve over cosmic time. The most massive galaxies arrive in the merger region first due to the contribution of bright satellites at early times. Lower mass galaxies reside in the non-merger region of $G - M_{20}$ and $C - A$ due to satellites at early times being too faint to be detected in the segmentation map. At later times, as the accretion rate increases and the contribution of satellites becomes more significant, the lower mass galaxies move into the merger regions.

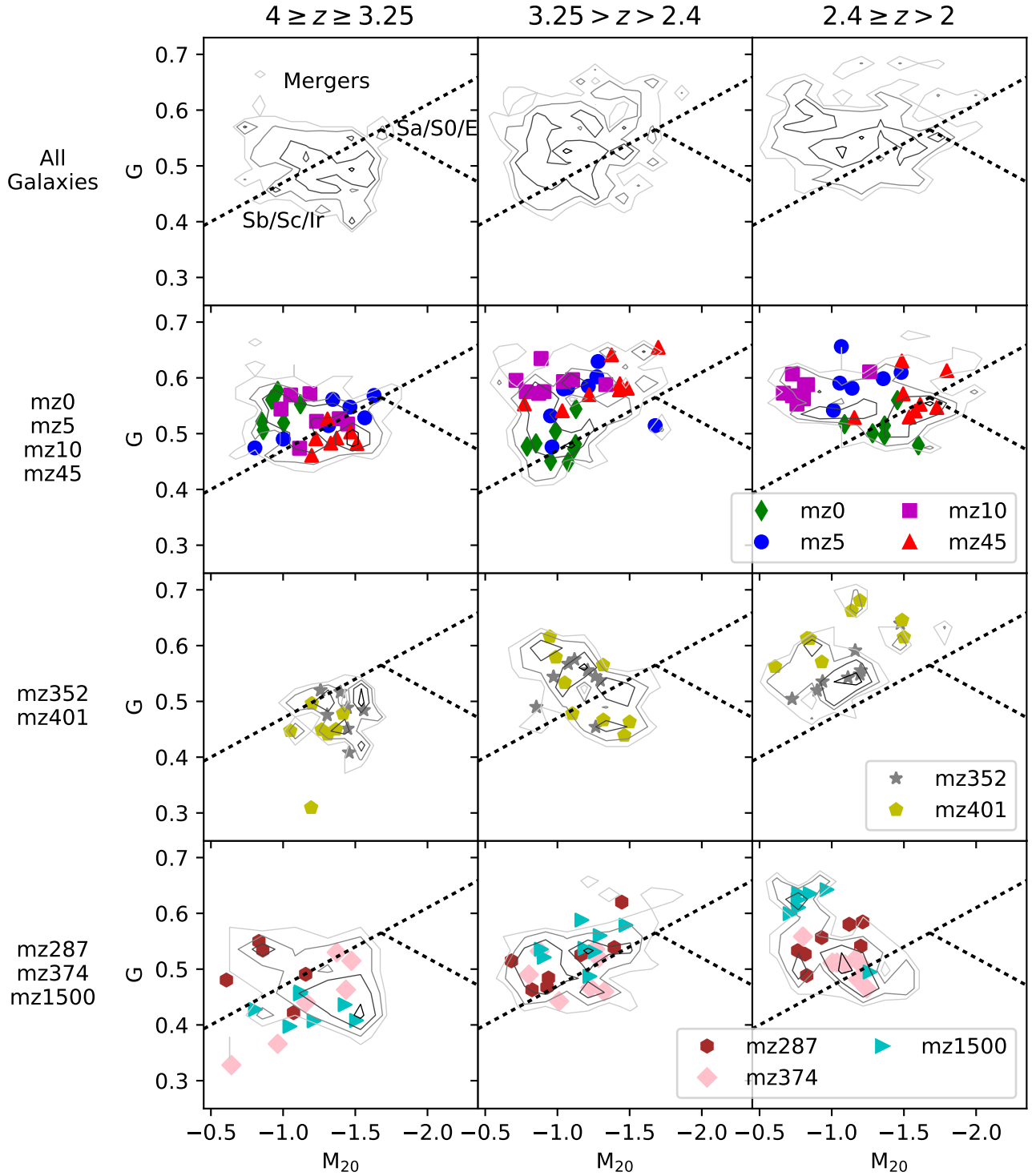


Figure 7. Location in $G - M_{20}$ space of the central galaxy in each simulation. The contours are spaced logarithmically from the second smallest non-zero number density value to the second largest value. The G and M_{20} markers are sightline medians (over the unique viewing angles) and the different shapes correspond to the different simulations which are given in Table 1. The labels indicate the Hubble Sequence classifications of local galaxies typically found in each region (Lotz et al. 2008b).

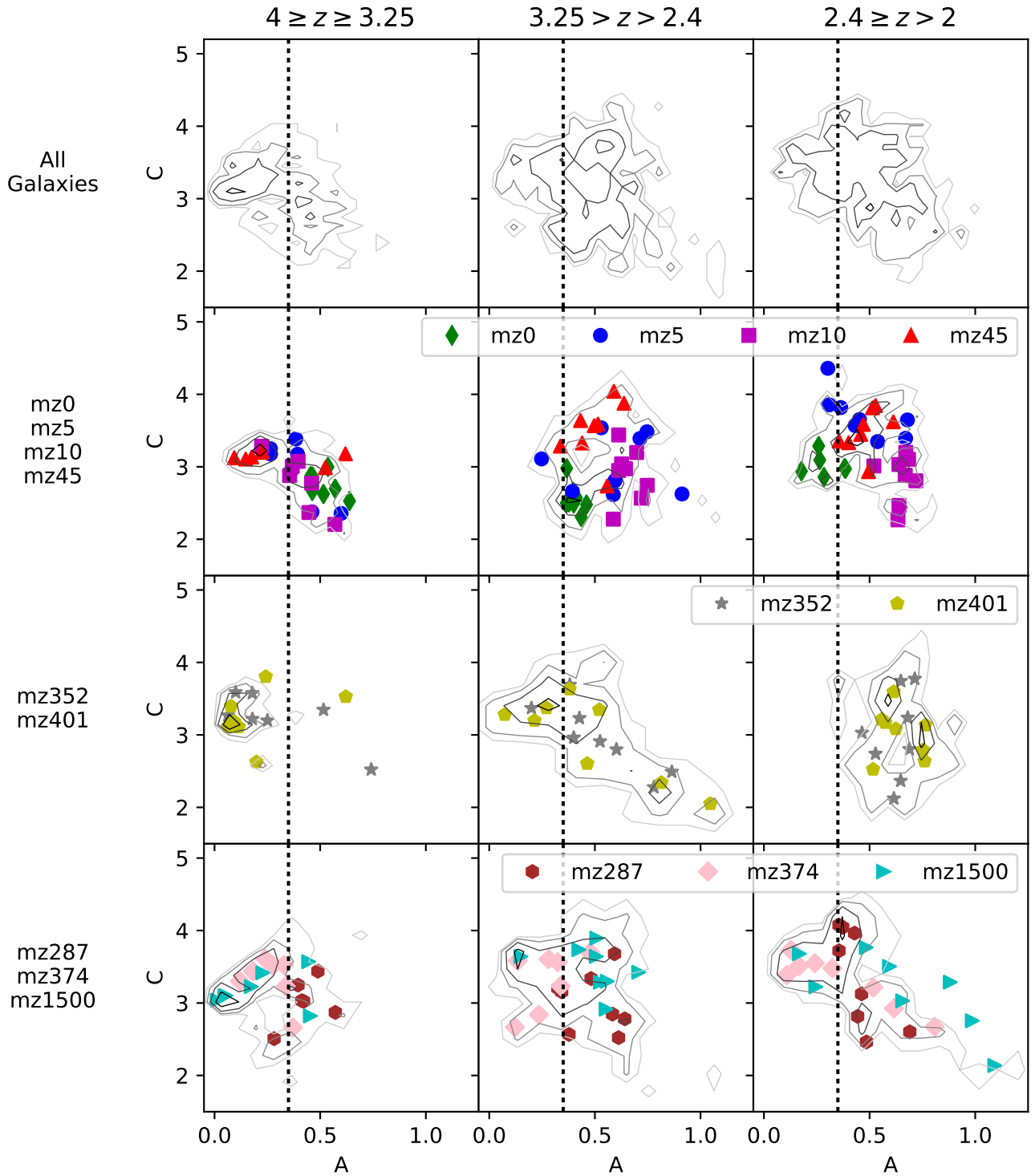


Figure 8. Location in $C - A$ space of the central galaxy in each simulation. Akin to Figure 7, the contours are spaced logarithmically from the second smallest non-zero number density value to the second largest value. Likewise, the markers are the sightline medians (over the unique viewing angles) and the different shapes correspond to the different simulations. The dashed line indicates a division in A values used to identify mergers in local galaxies (Conselice 2003); points to the right of the vertical dashed line typically indicate galaxy mergers.

In Figure 9, we quantify these trends with mass, and plot the evolution of the median $G - M_{20}$ merger statistic, and A with redshift. The $G - M_{20}$ merger statistic (also referred to in the literature as “mergyness”, e.g. Thompson et al. 2015) is defined as the perpendicular distance from the canonical $G - M_{20}$ merger line (i.e. $G = -0.14M_{20} + 0.33$), with more positive values being further in the merger region. Similarly, we plot the median A value, noting the canonical $A = 0.35$ line that defines mergers. We show, at the top, the location of major and minor mergers for each model. Nearly all galaxies show more signs of mergyness at lower redshift, though (as seen repeatedly now), more massive galaxies move to the merger regions of the $G - M_{20}$ and $C - A$ spaces earlier.

5 DISCUSSION

5.1 Utility of $G - M_{20}$ and A as diagnostics for mergers at $z \sim 2 - 4$

We begin our discussion with an extended study into the utility of $G - M_{20}$ and A in identifying galaxy mergers amongst massive galaxies at high-redshift. Fundamentally, we want to answer: how often are $G - M_{20}$ and A correctly reporting mergers, and how often do they incorrectly identify a galaxy as merging when it is not? Relatedly, we want to understand the fraction of time mergers may be missed by these metrics. Throughout this discussion we will keep returning to the same fundamental point: the complex environments surrounding massive galaxies at high-redshift force $G - M_{20}$ and A to be elevated for the bulk of the galaxy’s life, thus rendering the metrics unable to capture mergers on short time scales.

To understand this, the first item we should address is: how often are our galaxies actually merging? From the top panel of Figure 9, it is clear that both major and minor mergers are relatively frequent in galaxies of all masses, except the most massive halos (mz0, mz5). Quantitatively, every galaxy in our model mass range undergoes a merger at least every ~ 1 Gyr. We show this exactly in the bottom panel of Figure 10, where we bin our model galaxies into three mass bins, and plot the timescales after the last major merger for all of our model galaxies. Only for the most massive bin (i.e. the rarest galaxies) are there a few systems that go ~ 1.5 Gyr between mergers.

Understanding the typical cadence of major mergers is important because it informs an ideal feature of non-parametric galaxy mergers for galaxies at high ($z \gtrsim 2$) redshift: they must be able to reliably detect mergers on time scales $t_{\text{merger}} \ll 1$ Gyr. Once a galaxy approaches timescales ~ 1 Gyr since the last merger, it is almost guaranteed to undergo another merger again. Any merger classifier that only works on time scales comparable to the time between mergers in effect is then just tracing the entire galaxy population, and is thus of limited use.

5.1.1 The Utility of $G - M_{20}$ and $A \geq 0.35$: Post Merger Timescales

We first aim to understand the utility of non-parametric morphological metrics in terms of the time scale (Δt) since

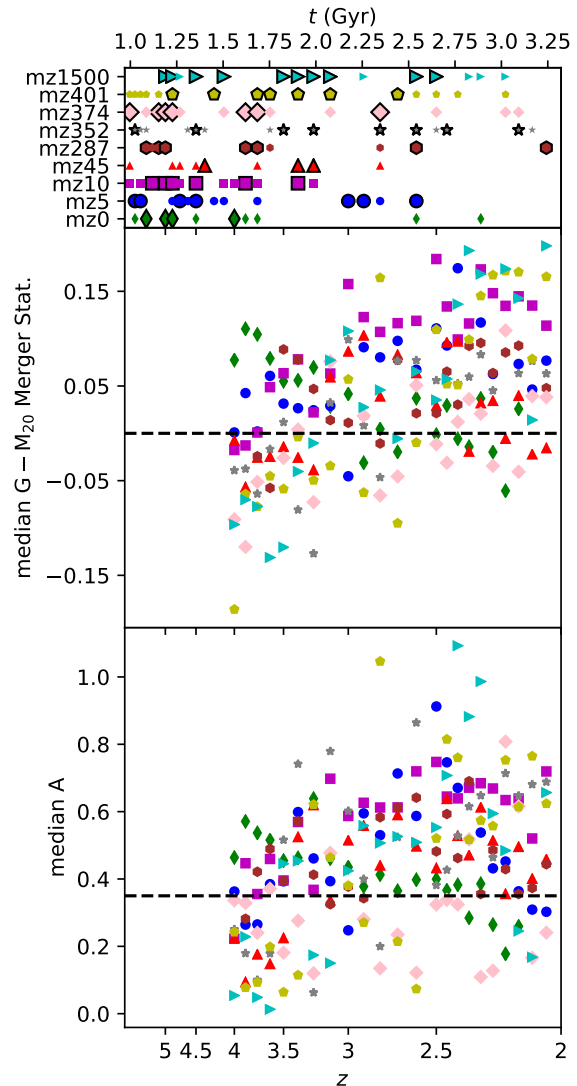


Figure 9. Evolution of merger diagnostics across z with indications of galaxy mergers. The upper panel illustrates mass increases indicative of galaxy merger. Larger markers with black outline correspond to a mass increase indicative of a major merger ($R \geq 0.25$), whereas smaller markers without an outline indicate mass increases indicative of minor mergers ($0.10 \leq R < 0.25$). The middle panel shows the median $G - M_{20}$ merger statistic vs. z for the central galaxy in each simulation. Likewise, the bottom panel shows the median A over z . The merger indicators were obtained by taking the median over all valid measurements at unique viewing angles at each z for each simulation. The different combinations of shapes and colours represent data from different simulations.

a major merger. To do this, we return to Figure 10, where we now highlight the top row. As a reminder, the galaxies are binned in three stellar mass bins whose bounds were chosen to distribute the snapshots where a mass increase indicating a merger as evenly as possible, with details of the bins in Table 3. We purposely omit 3 galaxies with $M_* \lesssim 10^{7.26} M_\odot$ because their inclusion would have made the distribution of galaxies more unequal. Note, unlike the previous section where we refer to the sizes of all galaxies in

Table 3. Descriptions of the M_* galaxy bins. Specifically, we list the number of snapshots between $4 \leq z < 2$ where there is a merger and at least one measurement of a diagnostic, and the total number of snapshots for which we make at least one measurement of a diagnostic.

$\log_{10}(M_*/M_\odot)$ Bins	$G - M_{20}$ mergers	A mergers	$G - M_{20}$ measurements	A measurements
[7.33, 8.55)	12	13	45	48
[8.55, 9.77)	10	10	64	65
[9.77, 10.99]	8	8	85	87

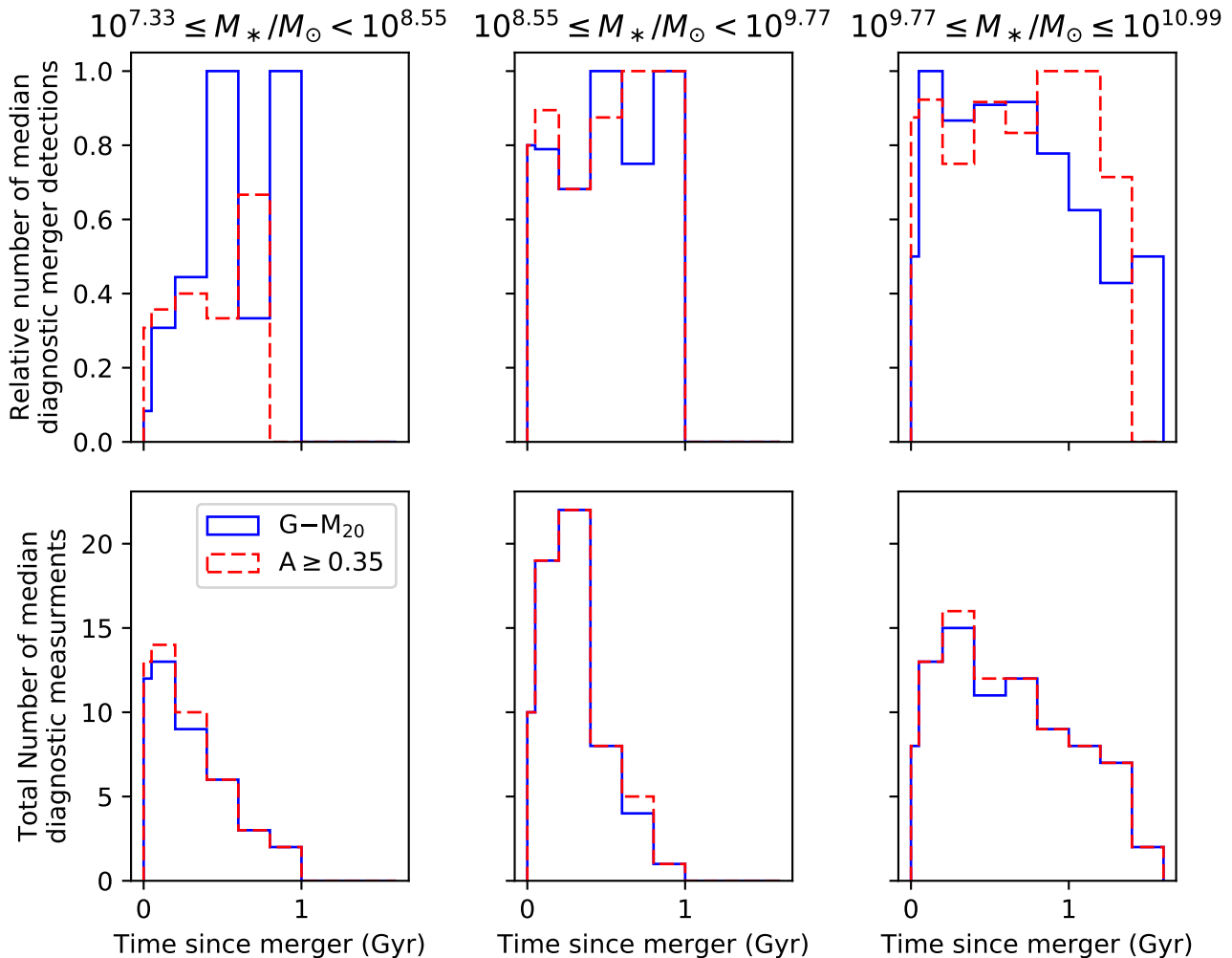


Figure 10. Fraction of median diagnostic merger detections (top panel) and total number of median diagnostic measurements (bottom panel) as a function of Δt , or the amount of time the diagnostic is measured after a mass increase indicative of major merger ($R \geq 0.25$). Our model galaxies are binned by stellar mass, with each column corresponding to a different mass bin. $G - M_{20}$ is shown in solid blue lines while $A \geq 0.35$ is indicated by dotted red lines. Each bin has a width of 0.2 Gyr except for the first two bins which extend from 0 Gyr to 0.05 Gyr and 0.05 Gyr to 0.20 Gyr. Note that the minimum amount of time between snapshots is ≈ 0.0513 Gyr and therefore the first bin only contains median diagnostic measurements at $-\Delta t = 0$ Gyr. Except for $G - M_{20}$ with high mass galaxies, neither diagnostic's sensitivity to merger detections discriminates between a galaxy's proximity in time to a merger.

a simulation based on the mass of the central galaxy in the simulation at $z \sim 2$, in this section we bin the galaxies based on the M_* it has at a given snapshot, entirely independent of which simulation it comes from.

The morphological statistics are sightline averages. The top row illustrates the fraction of snapshots in a given time

bin that register a merger diagnostic, while the bottom row shows the total number of galaxy $G - M_{20}$ and A measurements in a given time bin. Note, in the case of multiple mergers in rapid succession, we consider these as individual merger events. For example, if a given galaxy has a merger at time $T = 0$ Gyr, and then another one at $T = 0.3$ Gyr,

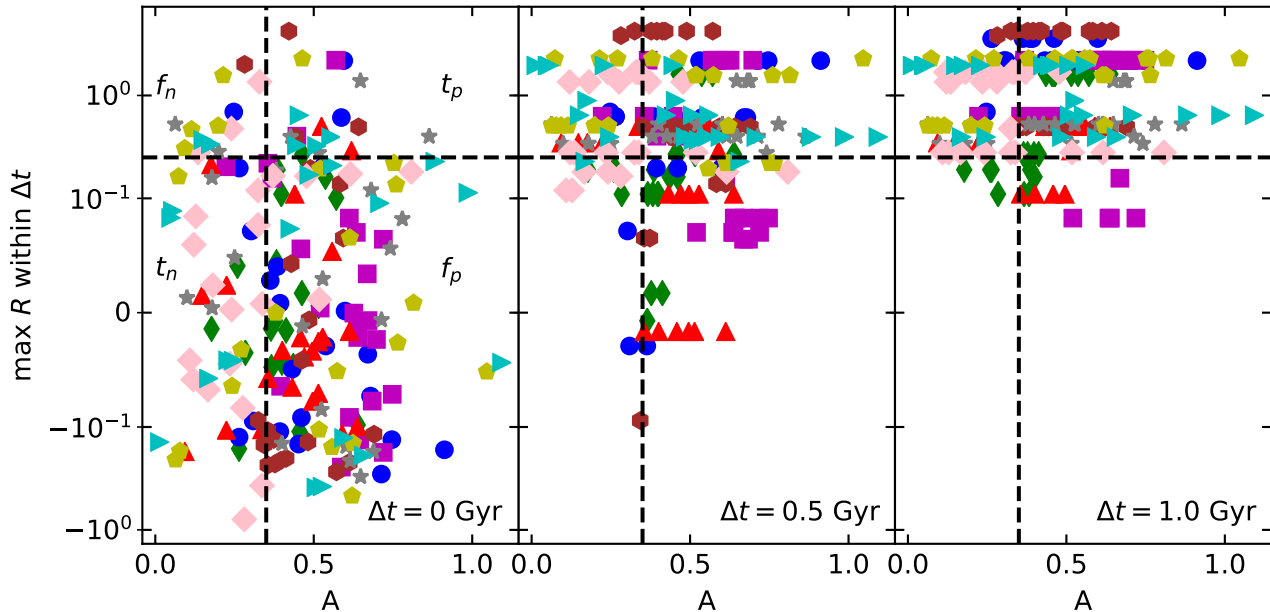


Figure 11. The maximum baryonic mass increase, R , at the time when the observation is measured or any earlier time within Δt , as a function of the sightline-median A for all simulations; Δt represents a potential timescale after a merger during which $A \geq 0.35$ might show heightened to detecting the merger. Each panel is labelled with the employed value Δt in the bottom right corner. The grid on each panel illustrate boundaries used to classify indications of galaxy mergers by A , using a threshold of $A \geq 0.35$ (the conventional threshold at low- z), for major mergers ($R > 0.25$), as true positives (t_p , upper right), false positives (f_p , lower right), false negatives (f_n , upper left) and true negatives (t_n , lower left).

then we will consider these as two separate merger events. The blue line denotes every time a galaxy would be classified as a merger via $G - M_{20}$, whereas the red line shows when it would be classified via $A \geq 0.35$.

Two salient points arise from Figure 10. First, at the lowest stellar masses, neither non-parametric method appears to work particularly well. Both $G - M_{20}$ and $A \geq 0.35$ detect $\sim 20 - 100\%$ of the mergers during a given Δt time bin, and these values are independent of the time since a merger. As we will show quantitatively shortly, if a galaxy is merging, within ~ 1 Gyr, both methods work roughly as well as randomly guessing. This trend may be partially explained by the compact size of the lowest M_* galaxies; typically these galaxies consist of a small, bright nucleus surrounded by a relatively uniform brightness envelope of light. Several of the panels during $z \sim 4 - 3.5$ in Figures C5-C8, illustrate how CAESAR’s FOF finder frequently associates under-dense outlying regions of stellar density with these galaxies, which do not appear in the visual morphology. Mergers may be detected when the outlying regions of the merging galaxies overlap, but before the densest regions interact. In other words, there is a delay between the merger and morphological disturbance. Once the main galaxies interact, their compact size cause them to coalesce relatively quickly. Because of the sensitivity of the diagnostics to small irregularities, minor mergers could also lead to detections of mergers. Additionally, this trend may also be partially explained by the incompleteness of our sample of low M_* galaxies.

Second, in the intermediate and larger mass bins ($M_* > 10^{8.5}$), the relative number of median diagnostic merger detections stays uniformly large ($\gtrsim 80\%$) during the entire

$\Delta t = 1$ Gyr timescale. This is despite the fact that the number of galaxies with large time lags since the last merger drops dramatically as $\Delta t \rightarrow 1$ Gyr. What this means is that both $G - M_{20}$ and $A \geq 0.35$ register nearly all mergers up to ~ 1 Gyr after the merger. At the same time, nearly every galaxy undergoes mergers on time scales $t < 1$ Gyr (bottom row of Figure 10). In other words, effectively *all galaxies at all times are within $\Delta t = 1$ Gyr after a merger*, and neither method is able to discriminate on the time since a merger. Therefore, that $G - M_{20}$ and $A \geq 0.35$ nearly always register galaxies as mergers within 1 Gyr means that they in effect are simply tracing all massive galaxies at high-redshift. This suggests a limited utility in these metrics.

Why do massive galaxies register as mergers for the majority of their lives? As discussed previously (c.f. §4.2) this is due to the fact that more massive galaxies have larger optical morphologies. When galaxies have larger optical morphologies, the source extraction algorithm is less likely to separately identify the central galaxy and satellites. As a result, the final segmentation maps are less likely to mask out infalling galaxies, and therefore include both merging galaxies. Both $G - M_{20}$ and $A \geq 0.35$ therefore register the merger more easily in more massive systems. Concurrently, more massive halos tend to have multiple ongoing mergers, and therefore are more likely to register as a merger via $G - M_{20}$ and $A \geq 0.35$ over multiple sightlines.

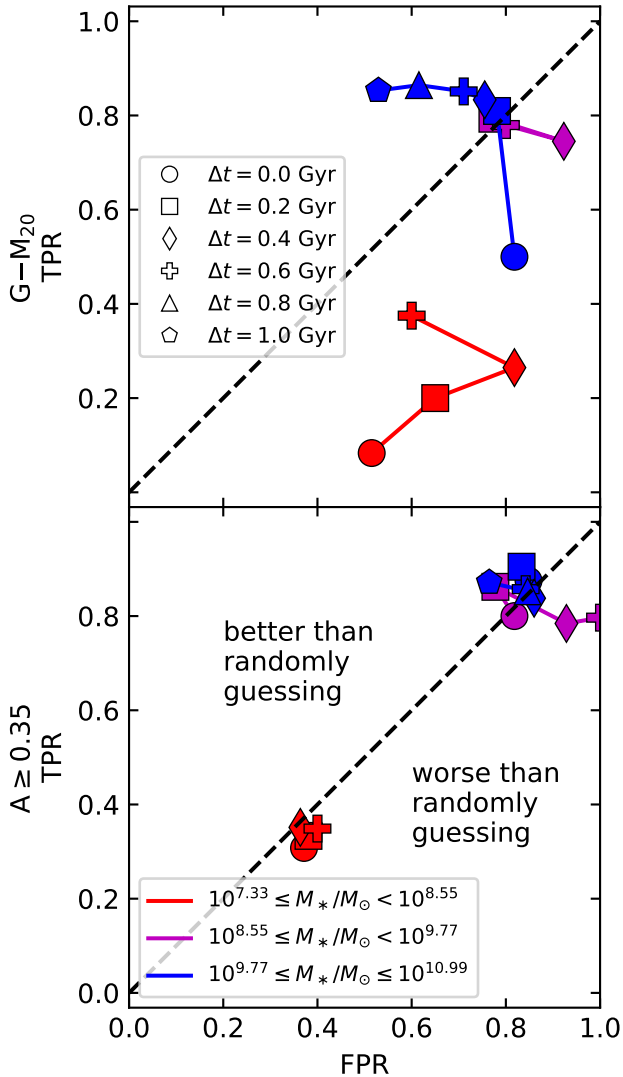


Figure 12. Utility of $G - M_{20}$ and $C - A$ as major merger indicators for high-redshift galaxies. We show this by computing ROC (Receiver Operating Characteristic) curves, or the median True Positive Rate (TPR) and average False Positive Rate (FPR) curve for sightline-median values of $G - M_{20}$ (top panel) and $A \geq 0.35$ (bottom panel) for identifying major galaxy mergers as functions of possible observability timescales Δt . The red, magenta, and blue curves are constructed from observations of low, intermediate and high M_* galaxies. Each point in a curve corresponds to the FPR and TPR at a given Δt which varies from 0 Gyr to 1.0 Gyr in 0.2 Gyr increments. We omit values for the low and intermediate M_* bins for $\Delta t \geq 0.8$ due to the dearth of observations of galaxies in those M_* bin more than 0.6 Gyr after the most recent major merger. Note that the $G - M_{20}$ point for galaxies in the intermediate M_* bin with $\Delta t = 0$ Gyr is almost directly below the point for galaxies in the intermediate M_* bin with $\Delta t = 0.2$ Gyr. In both panel, a black dashed runs along TPR=FPR. At a given point on line, (x, x) , the point represents the performance of randomly classifying x per cent of galaxies as undergoing a merger. **Except for the most massive galaxies and the longest post merger time scales, Δt , $G - M_{20}$ and A tend to perform comparably to randomly guessing.**

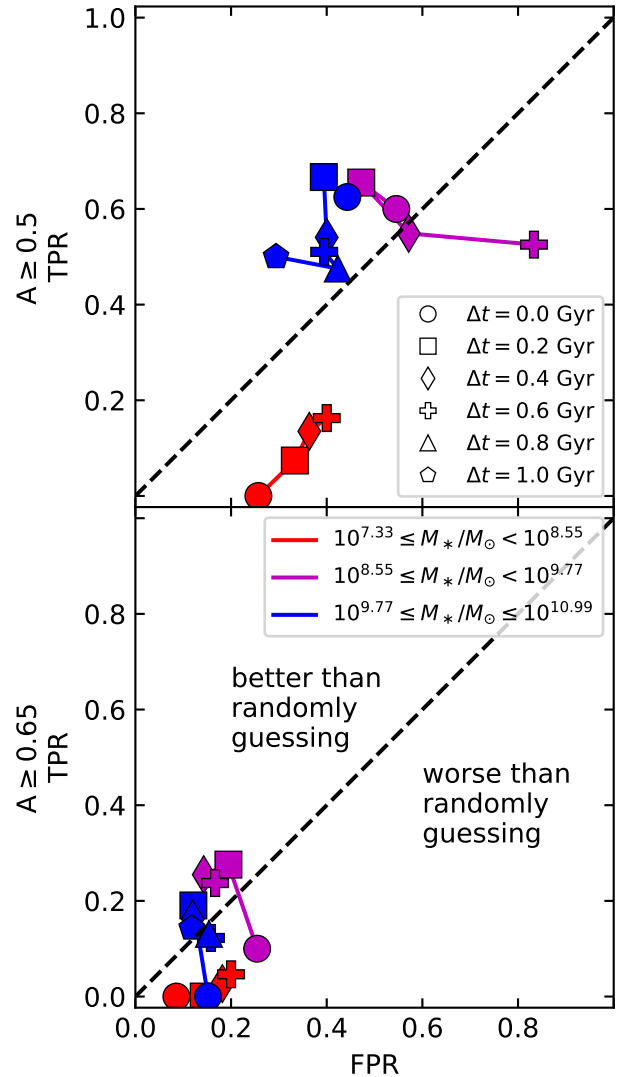


Figure 13. Like Figure 12 except it illustrates the utility of $A \geq 0.5$ and $A \geq 0.65$ as merger indicators for high-redshift major galaxy mergers. Other than $A \geq 0.5$ for intermediate and high M_* galaxies at selective time scales Δt , both A criteria perform comparably to randomly guessing.

5.1.2 The Utility of $G - M_{20}$ and $A \geq 0.35$: True and False Positive Rates

In the previous section, we demonstrated that both $G - M_{20}$ and $A \geq 0.35$ register mergers for significant periods of time following an actual merger event (up to ~ 1 Gyr). We now quantify the expected true and false positive rates of these morphological statistics.

We define two quantities. The True Positive Rate (TPR) is the fraction of all mergers that are detected by either $G - M_{20}$ or $A \geq 0.35$ within Δt . The False Positive Rate (FPR) is the fraction of snapshots within Δt that are incorrectly classified as mergers by the non-parametric measures.

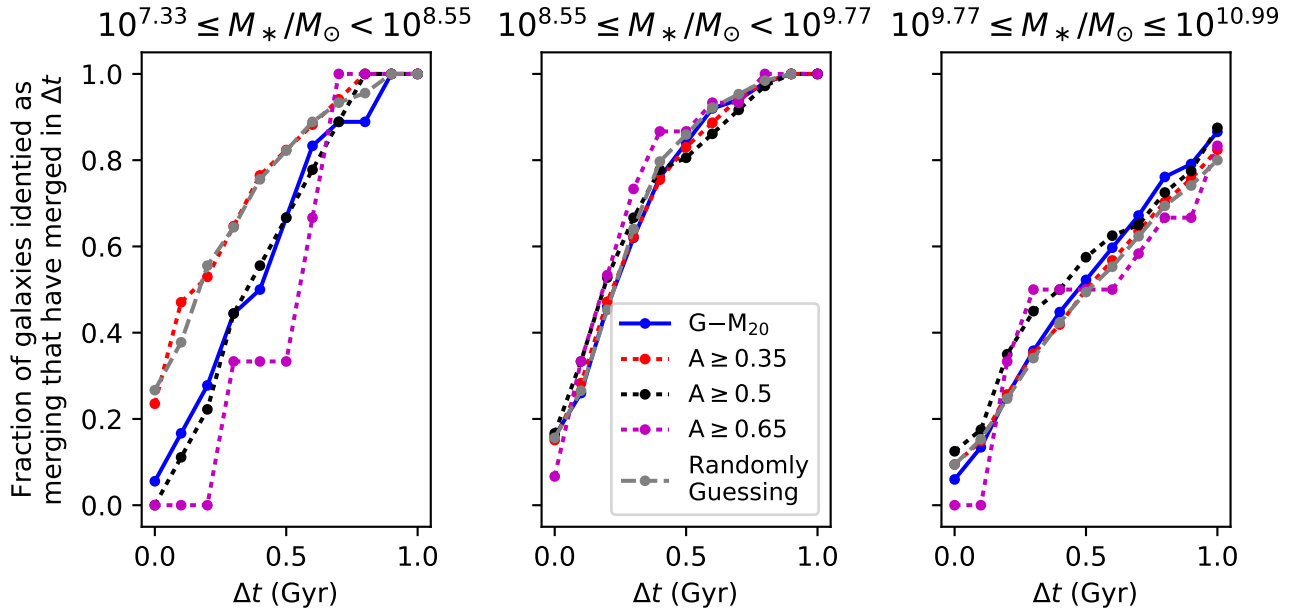


Figure 14. Fraction of systems identified as mergers that are actually mergers as a function of $\Delta t = 0$, or time after a merger. The blue solid line represents data for $G - M_{20}$ using the standard merger criteria. The dotted lines represent data for A while the different colours represent different thresholds; red represents $A \geq 0.35$ (standard), black represents $A \geq 0.5$ and magenta represents $A \geq 0.65$. The grey dashed line shows the fraction of systems identified as mergers if one randomly classifies $x\%$ of all galaxies as merging such that $0 < x < 100$. Each panel uses data for observations in which the central galaxy lies in a different M_* bin. There is no case where any diagnostic performs appreciably better than randomly guessing.

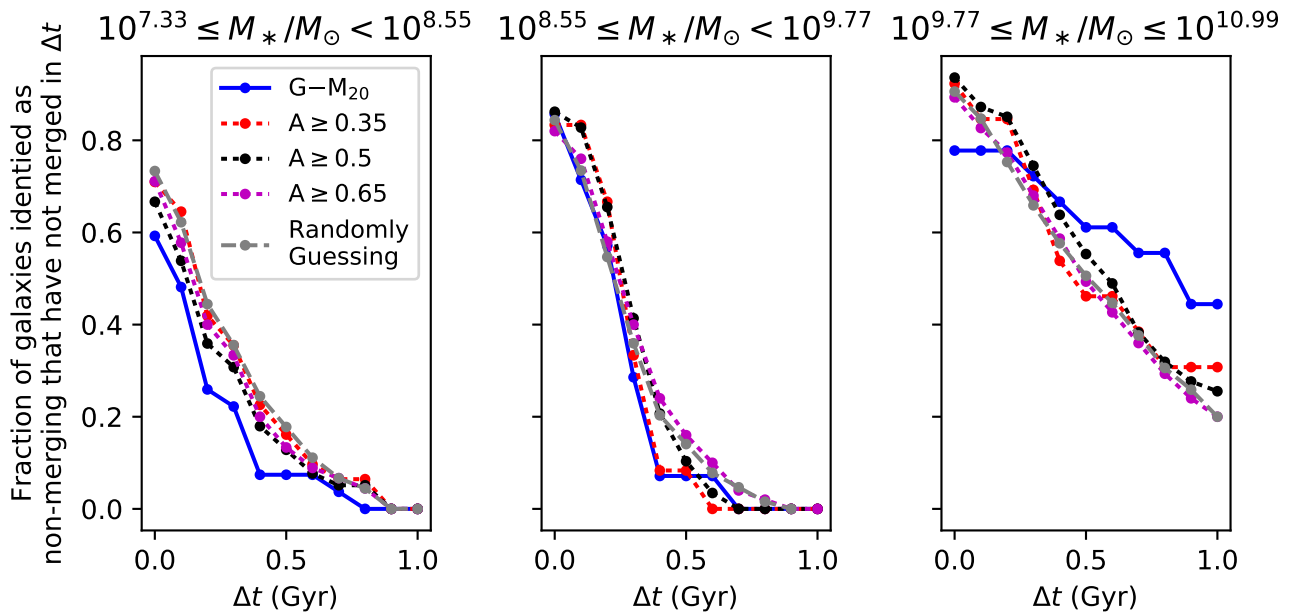


Figure 15. NPV (negative predictive value) of diagnostics as functions of Δt , or time after a merger. Diagnostics and diagnostic thresholds are represented by the same combinations of colours and lines as in Figure 14. The only instance where any diagnostic achieve considerably better performance than randomly guessing is $G - M_{20}$ for the galaxies in most massive M_* bin at a time scale Δt .

In other words:

$$\text{TPR} = \frac{t_p}{t_p + f_n} \quad (14)$$

$$\text{FPR} = \frac{f_p}{f_p + t_n} \quad (15)$$

where t_p and f_p are the number of true and false positives, respectively, and t_n and f_n are the number of true and false negatives, respectively. Note that $\text{TPR} + \text{FPR}$ does not necessarily equal 1. The TPR answers the question, "if a system is a merger, how often does a statistic identify it as a merger (within a time Δt)?"

We compute both fractions, for major mergers identified by median $G - M_{20}$ and A taken over individual sightlines of each snapshot, separately, using different values of Δt . It is important to note that each value of Δt fundamentally changes the definitions of what we consider a t_p , f_p , t_n and f_n . For example, if we increase Δt , we expect a diagnostic to detect a merger in a larger fraction of our mock observations, thereby converting some f_p into t_p , and some t_n into f_n .

To compute the number of true and false positives, we define $D_i(t)$ as the relative fraction of galaxies, in M_* bin i , identified as mergers Δt Gyr after a merger. We also define $G_i(t)$ as the distribution of galaxies in M_* bin i with the respect to the amount of time to the most recent major merger.

We can then compute the number of true and false positives directly from $G_i(t)$ and $D_i(t)$. Assuming that one observes N galaxies in M_* bin i and define the merger time scale as τ , then the t_p and f_p are given by

$$t_p = N \int_0^\tau G_i(t) D_i(t) dt \quad (16)$$

$$f_p = N \int_\tau^\infty G_i(t) D_i(t) dt \quad (17)$$

The equations for f_n and t_n are found by replacing $D_i(t)$ with $(1 - D_i(t))$ in the equations for t_p and f_p , respectively.

To build some intuition, in Figure 11, we show the distribution of our model galaxies that have true positive, true negative, false positive and false negative measurements. We only consider galaxies that undergo major mergers for simplicity, and for illustrative purposes, couch this in terms of $A \geq 0.35$ measurements. In Figure 11, each panel represents a different Δt value⁹. The ideal scenario is to have most of the model galaxy points in the top right (true positive; t_p) or bottom left (true negative; t_n) quadrants. Figure 11 clearly exhibits the expected trend we previously mentioned that as we increase Δt (i.e. as we move toward right most panel), galaxies tend to be converted from f_p into t_p , and t_n into f_n (i.e. they move to the top of each panel towards the t_p and f_n quadrants).

Figure 11 also demonstrates that A does not clearly correlate in any way with the underlying merger ratio. If A represented some measure of whether an object has recently undergone a merger, one might expect that it would be positively correlated with R . However, for no Δt does such a correlation appear. Although we do not show it here,

⁹ Note that this figure was only constructed with data back to $z \sim 5.6$, and consequently there is not a full Gyr of data before every observation; this effect is insignificant as there is a major merger in every simulation during $z = 5.6 - 4$.

a similar lack of correlation is seen for the $G - M_{20}$ merger statistic with R . This foreshadows that identifying mergers with quantitative morphological measures will not be easy. We next quantify this more precisely.

We now use the t_p and f_p metrics to ask, over what time scales are $G - M_{20}$ and $A \geq 0.35$ likely to produce true and false positives for a given mass bin. In Figure 12, we show this via a Receiver Operating Characteristic Curve. In the ROC, the axes are TPR and FPR, and the 1:1 line is plotted. The 1:1 line essentially signifies the division at which randomly guessing if a galaxy is merging would be better: above this line, the non-parametric measure performs better than randomly guessing. A point along that line, (x, x) indicates the performance randomly classifying x per cent of galaxies as undergoing a merger. For example, if a diagnostic has a TPR of 0.75 and an FPR of 0.75, the exact same result can be achieved by randomly classifying 75% of all observed galaxies as undergoing a merger. Within the ROC curves, we show three mass bins (signified by the three different colours), as well as six different time scales following a merger event.

In short, The ROC curves in Figure 12 demonstrate that at best, for most masses and most time scales Δt , $G - M_{20}$ and $A \geq 0.35$ perform comparably to randomly guessing. Only for the most massive time bin, and for the longest time scales do these metrics beat guessing. This is evident in Figure 10, where for the most massive time bin, the likelihood of $G - M_{20}$ detecting a merger a significant time (~ 1 Gyr) after a merger is relatively small. An elevated asymmetry cut of $A \geq 0.5$ performs a bit better than $A \geq 0.5$ for massive systems, as does $A \geq 0.65$.

While it is not shown here, we also examined the effectiveness of the statistics by combining Δt with $-\Delta t$ values of 0.1 Gyr and 0.2 Gyr (The inclusion of $-\Delta t$ in the calculations allowed us to ask if a given non-parametric morphology statistic can identify mergers *prior* to the snapshot where the stellar mass increase indicating a merger is measured). We ultimately found that this had neutral or negative effects on each of the ROC curve and have thus omitted it from our figures.

At face value, then, Figure 12 suggests that the usage of quantitative morphology measures at high-redshift (especially in the intermediate to low M_* regime) is complicated by the significant false positive rates in comparison to the true positive rates; with the exception of $G - M_{20}$ for the largest M_* bin large at large Δt , the diagnostics are unable to discriminate between merging and non-merging galaxies. This is simply a recasting of the results seen in Figure 10 – on average, except for the most massive galaxies and longest time scales, one may as well randomly guess if a galaxy is merging or not.

It is worth noting, however, that there is a significant uncertainty in our calculated false positive rate. As a reminder, we have discarded all sightlines that either have poor SNR ($\langle SNR \rangle < 20$), or non-contiguous segmentation maps. In particular, while relatively few sightlines for $C - A$ data are discarded, $G - M_{20}$ values that come from rather abnormal morphologies can sometimes result in either background pixels that lower the signal to noise ratio, or non-contiguous segmentation maps. As a result, $G - M_{20}$ values from observations following a merger and observation of very compact

galaxies are particularly likely to be discarded, thus lowering the total number of true positives registered in Figure 12.

In Appendix D we illustrate the uncertainty associated with our measurements by regenerating Figure 12 and at every timescale, assume that all of the discarded measurements have values that are the most optimistic for each diagnostic's performance. Figure D1 demonstrates that despite this, the results for $A > 0.35$ are unchanged. The results for $G - M_{20}$, however, can be greatly improved by including sightlines that have non-contiguous segmentation maps or low SNR detections. We suggest, however, that this is a somewhat unrealistic scenario as it requires including data that would otherwise be discarded for quality issues. In summary, $G - M_{20}$ performs best at diagnosing merging large M_* galaxies at $\Delta t \sim 1.0$ Gyr. This is the only case in which a conventional diagnostic appears to definitively work significantly better than randomly guessing. A works comparably to randomly guessing for most masses and post-merger timescales.

5.1.3 Utility of alternative A criteria

While examining the full $G - M_{20}$ space for potentially better merger criteria is outside the scope of this work, we briefly examine a small number of more stringent Asymmetry criteria in Figure 13. In Figure 13 we illustrate ROC curves for $A \geq 0.5$ and $A \geq 0.65$ at a variety of Δt for each of the three M_* bins.

Essentially, the ROC curves in Figure 13 illustrates how for most time scales and masses both A criteria performs comparably to randomly guessing, at best. The only cases in which either criteria is substantially superior to randomly guessing is $A \geq 0.5$ for intermediate to most massive M_* bin with a timescale $\Delta t \sim 0.2$ Gyr.

Similar to $G - M_{20}$ for high M_* galaxies with $\Delta t = 1.0$ Gyr, $A \geq 0.5$ for both intermediate to high M_* galaxies with $\Delta t = 0.2$ Gyr, has a relatively high probability of detecting mergers at immediately after a galaxy merges that decreases substantially around its optimal Δt . However, for galaxies in the intermediate (high) M_* bin, $A \geq 0.5$ shows a spike in the probability of detecting mergers greater than (comparable to) the probability of detecting mergers less than 0.2 Gyr after the merger. This spike occurs for galaxies that have not merged in 0.6-1.0 Gyr (0.6-0.8 Gyr after which it decreases again). Because this spike in probability occurs in time bins that contain $\sim 17\%$ ($\sim 14\%$) of all galaxies in a given bin that have not merged in at least 0.2 Gyr, the average probability of $A \geq 0.5$ identifying a galaxy less than 0.2 Gyr after a merger is greater than that for a galaxy more than 0.2 Gyr after a merger.

5.2 Questions of Interest

Thus far, we have discussed the performance of $G - M_{20}$, $A \geq 0.35$, $A \geq 0.5$, $A \geq 0.65$ as merger diagnostics. We have concluded that there are only two cases where a diagnostic performs substantially better than randomly guessing:

- (i) $G - M_{20}$ on timescales of $\Delta t \sim 1$ Gyr for high M_* galaxies
- (ii) $A \geq 0.5$ on timescales of $\Delta t \sim 0.2$ Gyr for intermediate to high M_* galaxies.

We will use the results we have developed so far to answer questions targeted questions that may be of use to observational surveys.

5.2.1 Is my observed galaxy undergoing a merger right now?

What is the probability that any given observed galaxy is undergoing a galaxy merger, based on the results of $G - M_{20}$ or A diagnostics? To answer this, we measure the probability that a galaxy with a merger diagnostic indicating a merger comes from a snapshot where $R \geq 0.25$ (we effectively measuring the probability for $D_i(t = 0)$).

The specific metric with which we can measure this probability is called PPV (positive predictive value), or precision, which is given by

$$\text{PPV} = \frac{t_p}{t_p + f_p}. \quad (18)$$

In other words, PPV measures the ratio of true positives to all positive signals. A PPV = 100% is ideal. In Figure 14, we plot the PPV as a function of Δt for each M_* bin using the median diagnostic value taken over all unique lines of sight for a given snapshot. To answer this question we only care about the values of PPV when $\Delta t = 0$.

The values of PPV are sensitive to the distribution of galaxies as a function in time after the merger. To illustrate the effects of the underlying distribution of galaxies on the PPV, we include a curve in Figure 14 that shows the PPV for randomly identifying galaxies with probability x . One can show, that as long as x satisfied $0 < x < 1.0$ its PPV is entirely determined by the underlying distribution of galaxies.

From Figure 14, we find that each of the A thresholds and $G - M_{20}$ have PPVs ranging from 0 to ~ 0.20 at $\Delta t = 0$. In other words there is less than a 20 per cent chance that a galaxy is undergoing a merger right now. In nearly all cases, one can identify a larger or comparable fraction of merging galaxies by randomly guessing.

5.2.2 Has my observed galaxy undergone a merger within a characteristic timescale, Δt ?

We again turn to Figure 14 to determine this answer. We see that as Δt increases, so does the precision of each diagnostic. While there is more dispersion in the PPV of the diagnostic at lower Δt , the precision appears to converge at ≥ 0.6 Gyr. That said, it is important to note that the upward trend with Δt is expected. As we increase the Δt , f_p are converted into t_p (e.g. Figure 12). Therefore, as Δt is increased the precision can only get better or remain the same.

We find that for galaxies in the largest M_* bin, about 85 per cent of galaxies identified as merging by $G - M_{20}$ have merged within a $\Delta t \sim 1.0$ Gyr. For galaxies in the intermediate (high) M_* bin, about 55 (35) per cent of galaxies with $A \geq 0.5$ have merged within ~ 0.2 Gyr.

5.2.3 Is a galaxy identified as non-merging actually not merging?

This question is quantitatively answered by NPV (negative predictive value) which is defined as

$$\text{NPV} = \frac{t_n}{t_n + f_n}. \quad (19)$$

In other words, NPV is the fraction of all negative signals (i.e. when $G - M_{20}$ and A diagnostics say that a galaxy is not merging) that are truly not merging. Figure 15 illustrates NPV as a function of Δt since the most recent major galaxy for each M_* bin. It is critical to consider NPV alongside PPV. Like PPV, NPV is also highly dependent on the underlying distribution of galaxies with time after a merger. To illustrate this dependence, we include the NPV in Figure 15 for randomly identifying x per cent of galaxies as merging, such that $0 < x < 100$.

From Figure 15, we find that NPV decreases as Δt increases. This is expected because as we increase Δt , t_n are converted into f_n (e.g. Figure 12; consequentially NPV can only get worse or remain the same. Additionally, Figure 15 shows that within a M_* bin, all of the A merger criteria evolve similarly. We also find while $G - M_{20}$ evolves relatively similarly to A in the low and intermediate M_* bin, in the most massive M_* bin, the NPV of $G - M_{20}$ decreases with a much shallower slope than that of A .

Figure 15 indicates that ~ 45 per cent of galaxies in the most massive M_* bin identified by $G - M_{20}$ as non-merger have actually merged in the last Gyr. The figure also demonstrates how ~ 65 (~ 85) per cent of galaxies in the intermediate (high) M_* bin with $A < 0.5$ have not merged within the previous ~ 0.2 Gyr.

Considering both the PPV and NPV together, we conclude that $A > 0.5$ is not a particularly useful diagnostic for identifying galaxy mergers at high z . We find that $A > 0.5$ does not achieve considerably better performance than randomly guessing in terms of PPV and NPV for galaxies in both the intermediate and highest M_* bins. The fact that $A \geq 0.5$ has a larger NPV than PPV suggests that it may be used to remove galaxies from a sample that have not merged within the last 0.2 Gyr. Then in principle, other methods could be employed to identify which of the remaining sample of galaxies actually merged. Unfortunately, $A \geq 0.5$'s utility in screening out galaxies that have not merged in 0.2 Gyr is limited by its TPR of ~ 0.65 (see Figure 13); about 35% of galaxies that merged in the last 0.2 Gyr would be screened out in the process.

On the other hand, for the largest M_* galaxies at the longest time scale, $\Delta t = 1.0$ Gyr, $G - M_{20}$ has a NPV approximately double that of randomly guessing and a PPV comparable to that of randomly guessing. Due to its long time scale of activity, the main use of $G - M_{20}$ would be to identify high M_* galaxies that have not merged in the last Gyr. The absolute value $G - M_{20}$'s NPV ($\sim 45\%$) considerably limits the utility of $G - M_{20}$ (despite being twice as large as that of guessing); more than half of all high M_* galaxies that do not meet the $G - M_{20}$ merger criterion have undergone a merger in the last Gyr. While an argument could be made for using $G - M_{20}$ to screen out merging galaxies, this is not particularly relevant to how well $G - M_{20}$ identifies mergers.

5.3 Comparison to other Theoretical Studies

In the last decade, several authors have sought to utilize numerical simulations to study quantitative morphology measures. These studies span a diverse range of methods, ranging from (i) studying the morphologies idealised galaxy merger simulations (e.g. Lotz et al. 2008a, 2010a,b); (ii) studying the morphological measures in of galaxies from a collection of cosmological zoom simulations (e.g. Hambleton et al. 2011; Snyder et al. 2015a); and (iii) studying the morphological measures for a statistically large sample of mock observations generated from coarser resolution large-box cosmological simulations (e.g. Snyder et al. 2015b; Bignone et al. 2017). In all studies from the first two categories, the mock observations were generated with full Monte Carlo dust radiative transfer simulations (Lotz et al. 2008a, 2010a,b; Snyder et al. 2015a), while studies in the third classification use mock observations from the Illustris Project (Snyder et al. 2015b; Bignone et al. 2017), which were generated with radiative transfer simulations that omit the effects of dust (Torrey et al. 2015) emission. Because our work falls into the second category and has many similarities to works in the first category, we primarily focus our comparison works in these categories.

Lotz et al. (2008a) were the first to study morphological measures in numerical galaxy formation simulations. These authors utilised a combination of SUNRISE dust radiative transfer (Jonsson 2006; Jonsson & Primack 2010; Jonsson et al. 2010) with idealised galaxy merger simulations in order to generate mock observations of galaxies. Lotz et al. studied the dependence of $G - M_{20}$, CAS on a variety of factors for equal mass binary mergers including merger orbital parameters and orientation, viewing angle, dust, image resolution, gas fraction, scale length, and different models of supernova feedback. In Lotz et al. (2010a) and Lotz et al. (2010b), the same group employed similar methods to study the dependence of morphological measures on the mass ratio and gas fractions of the merging galaxies, respectively. In each of these papers they analysed the average observability timescales on which $G - M_{20}$ and A identify mergers of local galaxies. Their observability time scale measures the line-of-sight averaged total amount of time that a diagnostic indicates disturbed morphologies for **both** pre-merging galaxies and the post-merger system; our merger time scale, Δt measures a fundamentally different quantity. While a direct comparison of our models to theirs is not straightforward, owing to the messy complex environments that surround high- z massive galaxies in cosmological simulations (as compared to the relatively cleaner environments of idealised binary mergers), in Appendix B, we apply our methods to an idealised binary galaxy merger simulation and find comparable results to these previous works.

Hambleton et al. (2011) studied the CAS morphology of a collection of $z = 0$ simulated galaxies in zoom simulations, and compared the morphology trends to that of the Frei et al. (1996) catalogue of local galaxies. Using SUNRISE, they generated mock observations at $z = 0$ for a collection of 15 galaxies simulated with GASOLINE (Wadsley et al. 2004) cosmological zoom simulations. This collection contained 12 galaxies with masses similar to that of the Milky Way and 3 galaxies with masses similar to that of the masses of dwarf Galaxies. These authors, concentrating on understanding

the $C - A$ diagnostic, found galaxies that typically found comparable concentration indices as observed local galaxies, though model galaxies that have significantly higher A values.

Snyder et al. (2015a) used SUNRISE to generate mock observations of galaxies, from ART (Kravtsov et al. 1997; Kravtsov 2003) cosmological zoom simulations, that closely mimic the resolution, depth, filters, and noise of the *HST* observations from the CANDELS-Wide survey (Grogin et al. 2011). Unlike in our analysis where we study the quantitative morphological measures computed from the observations in the rest-frame B filter with $\langle SNR \rangle \geq 20$ along 13 lines of sight, they examined the morphologies in the closest *HST* filter to the rest-frame B filter with a selection criteria of $H < 24.5$ along 5 lines of sight. Snyder et al. (2015a) studied the evolution of the morphology of 10 simulated galaxies, with $10^{9.2} \leq M_*/M_\odot \leq 10^{10.3}$ (at $z \sim 2$), from $z \sim 3.5$ to $z \sim 0.7$. Additionally, they also examine the timescales on which $G - M_{20}$ and MID are sensitive to a mergers for 3 galaxy simulations in which a single major or minor merger occurs at $z \lesssim 2.2$ (Snyder et al. 2015a).

Our simulation sample generally spans larger masses at high-redshift than the Snyder et al. (2015a) work, though there is some overlap in our low-mass regime and their high-mass end. Similar to these authors, we see an increase in r_p with decreasing redshift for our model galaxies. We additionally see a similar dynamic range in measured G values, with particularly good agreement from mz287 and mz374 at $z \sim 2$. However, our model M_{20} extends over a much larger range of values (and, broadly, larger values). This discrepancy forces our model galaxies, on average, to reside in the merger region of $G - M_{20}$ while those from the Snyder et al. (2015a) work typically are not at the same redshift.

This difference may be physical. As demonstrated in Appendix B, our radiative transfer and source detection algorithms result in similar results as comparison models when performing apples-to-apples tests. At the same time, while the low mass models in our simulation sample tend toward merger regions in $G - M_{20}$ and $C - A$ space at late ($z \approx 2$) times, these galaxies also have relatively larger merger rates (c.f. Figure 6). It may be that our model galaxies that share an overlapping mass range with those studied in Snyder et al. (2015a) undergo a richer merger history during the redshift range of interest.

6 CONCLUSIONS

We have analysed the effectiveness of quantitative morphological measures G , M_{20} , C and A in galaxies at high-redshift ($z = 2 - 4$) by combining a series of cosmological zoom simulations of galaxy formation with dust radiative transfer models in order to create mock observations of galaxies. Our results focus on galaxies ranging from proto-Milky Way mass through relatively high ($M_{\text{halo}} \approx 10^{13} M_\odot$ at $z = 2$). Our primary results follow.

(i) Galaxies tend to move from the “non-merger” (e.g. Sb/Sc/Ir) region of $G - M_{20}$ space to the “merger” region with cosmic time. Higher mass galaxies transition from the non-merger \rightarrow merger region at earlier times, followed by lower mass galaxies at lower redshifts. A similar effect is true in $C - A$ space.

(ii) Generally, $G - M_{20}$ and $A \geq 0.35$ tend to accurately identify most major mergers at high-redshift in the intermediate to high M_* galaxies within our modeled mass range. Galaxies in the most massive have a large merger rate at early times ($z \gtrsim 4$), while the galaxies in the less massive simulations have increased merger rates at later times. These are both reflected in the $G - M_{20}$ and $A \geq 0.35$ values.

(iii) At the same time, there is a significant false positive rate, relative to the true positive rate in both $G - M_{20}$ and $C - A$ space, complicating the interpretation of these metrics. These false positive rates are due to the highly complex environments characteristic of massive galaxies at high-redshift. Subhalos surrounding the central galaxy distort the final segmentation maps, causing increased G and A values, even when a galaxy is not actively merging.

(iv) On average, both $G - M_{20}$ and $A \geq 0.35$ perform comparably to randomly guessing if a galaxy is merging or not. The main exception to this is the most massive galaxies ($M_* \sim 10^{10} M_\odot$) on the longest post-merger time scales ($\Delta t \sim 1$ Gyr).

(v) In most cases other A merger thresholds, $A \geq 0.5$ and $A \geq 0.65$, achieve slightly better performance than $A \geq 0.35$. However the only cases where either threshold achieves significantly better performance than randomly guessing whether a galaxy is merger is $A \geq 0.5$ on a post-merger timescale of $\Delta t \sim 0.2$ Gyr for intermediate mass ($M_* \sim 10^9 M_\odot$) and the most massive galaxies.

These effects taken together suggest that the application of traditional non-parametric galaxy morphology measures for galaxy mergers to high-redshift galaxies may simply trace the complex environments of massive halos. These systems will typically eventually merge, but it is not straightforward to interpret these measures as reflective of ongoing active mergers.

ACKNOWLEDGEMENTS

The authors are grateful to J. Lotz for providing the code used to compute morphological measures for idealize galaxy mergers (Lotz et al. 2008a, 2010a,b) and to L. Bignone for providing data from his recent paper in digital format (Bignone et al. 2017). We thank Greg Snyder and Paul Torrey for helpful conversations. The code used to analyse data for this paper used NUMPY (van der Walt et al. 2011), CYTHON (Behnel et al. 2011), and MATPLOTLIB (Hunter 2007). M.A. acknowledges support from the Haverford College Koshland Integrated Natural Sciences Center. D.N. was partially supported by NSF AST-1724864, AST-1715206, and HST AR-15043.0001. The simulations for this paper were conducted on the Fock cluster at Haverford College, and the HiPerGator2.0 facility at the University of Florida. M.A. and D.N. thank Joe Cammisa at Haverford College for his efforts in maintaining the Fock cluster.

References

- Barbary K., 2016, *The Journal of Open Source Software*, 1
- Barnes J. E., Hernquist L., 1992, *ARA&A*, 30, 705
- Barton E. J., Geller M. J., Kenyon S. J., 2000, *ApJ*, 530, 660

- Behnel S., Bradshaw R., Citro C., Dalcin L., Seljebotn D. S., Smith K., 2011, *Computing in Science & Engineering*, 13, 31
- Behroozi P. S., Wechsler R. H., Conroy C., 2013, *ApJ*, 770, 57
- Bershady M. A., Jangren A., Conselice C. J., 2000, *AJ*, 119, 2645
- Bertin E., Arnouts S., 1996, *A&AS*, 117, 393
- Bignone L. A., Tissera P. B., Sillero E., Pedrosa S. E., Pellizza L. J., Lambas D. G., 2017, *MNRAS*, 465, 1106
- Casey C. M., et al., 2009, *MNRAS*, pp 1231–+
- Casey C. M., Narayanan D., Cooray A., 2014, *Physics Reports*, 541, 45
- Cassata P., et al., 2005, *MNRAS*, 357, 903
- Conroy C., Gunn J. E., 2010, *ApJ*, 712, 833
- Conselice C. J., 2003, *ApJS*, 147, 1
- Conselice C. J., 2014, *ARA&A*, 52, 291
- Cox T. J., Di Matteo T., Hernquist L., Hopkins P. F., Robertson B., Springel V., 2006a, *ApJ*, 643, 692
- Cox T. J., Dutta S. N., Di Matteo T., Hernquist L., Hopkins P. F., Robertson B., Springel V., 2006b, *ApJ*, 650, 791
- Cox T. J., Jonsson P., Somerville R. S., Primack J. R., Dekel A., 2008, *MNRAS*, 384, 386
- Davé R., Finlator K., Oppenheimer B. D., Fardal M., Katz N., Kereš D., Weinberg D. H., 2010, *MNRAS*, 404, 1355
- Davé R., Thompson R., Hopkins P. F., 2016, *MNRAS*, 462, 3265
- Davé R., Rafeferantsoa M. H., Thompson R. J., Hopkins P. F., 2017, *MNRAS*,
- Dekel A., et al., 2009a, *Nature*, 457, 451
- Dekel A., et al., 2009b, *Nature*, 457, 451
- Dunlop J. S., et al., 2017, *MNRAS*, 466, 861
- Dwek E., 1998, *ApJ*, 501, 643
- Elbaz D., et al., 2011, *A&A*, 533, A119
- Ellison S. L., Mendel J. T., Scudder J. M., Patton D. R., Palmer M. J. D., 2013, *MNRAS*, 430, 3128
- Engel H., et al., 2010, *ApJ*, 724, 233
- Fanning D., 2002, *Coyote's Guide to IDL Programming*
- Feldmann R., Hopkins P. F., Quataert E., Faucher-Giguère C.-A., Kereš D., 2016, *MNRAS*, 458, L14
- Finlator K., Davé R., Papovich C., Hernquist L., 2006, *ApJ*, 639, 672
- Freeman P. E., Izbicki R., Lee A. B., Newman J. A., Conselice C. J., Koekemoer A. M., Lotz J. M., Mozena M., 2013, *MNRAS*, 434, 282
- Frei Z., Guhathakurta P., Gunn J. E., Tyson J. A., 1996, *AJ*, 111, 174
- Gabor J. M., Capelo P. R., Volonteri M., Bournaud F., Bellovary J., Governato F., Quinn T., 2016, *A&A*, 592, A62
- Geach J. E., et al., 2016, *ApJ*, 832, 37
- Grogin N. A., et al., 2011, *ApJS*, 197, 35
- Guo Q., White S. D. M., 2008, *MNRAS*, 384, 2
- Hahn O., Abel T., 2011, *MNRAS*, 415, 2101
- Hambleton K. M., Gibson B. K., Brook C. B., Stinson G. S., Conselice C. J., Bailin J., Couchman H., Wadsley J., 2011, *MNRAS*, 418, 801
- Hayward C. C., Kereš D., Jonsson P., Narayanan D., Cox T. J., Hernquist L., 2011, *ApJ*, 743, 159
- Hayward C. C., Torrey P., Springel V., Hernquist L., Vogelsberger M., 2013a, arXiv/1309.2942,
- Hayward C. C., Narayanan D., Kereš D., Jonsson P., Hopkins P. F., Cox T. J., Hernquist L., 2013b, *MNRAS*, 428, 2529
- Hopkins P. F., 2015, *MNRAS*, 450, 53
- Hopkins P. F., Hernquist L., Martini P., Cox T. J., Robertson B., Di Matteo T., Springel V., 2005, *ApJ*, 625, L71
- Hopkins P. F., et al., 2009, *MNRAS*, 397, 802
- Hopkins P. F., Cox T. J., Hernquist L., Narayanan D., Hayward C. C., Murray N., 2013, *MNRAS*, 430, 1901
- Hubble E. P., 1926, *ApJ*, 64
- Hunter J. D., 2007, *Computing in Science & Engineering*, 9, 90
- Iverson R. J., et al., 2013, *ApJ*, 772, 137
- Jones E., Oliphant P., Peterson P., et al., 2001–, SciPy: Open source scientific tools for Python, <http://www.scipy.org/>
- Jonsson P., 2006, *MNRAS*, 372, 2
- Jonsson P., Primack J. R., 2010, *New Astron.*, 15, 509
- Jonsson P., Groves B. A., Cox T. J., 2010, *MNRAS*, 403, 17
- Kartaltepe J. S., et al., 2015, *ApJS*, 221, 11
- Kocevski D. D., et al., 2012, *ApJ*, 744, 148
- Koprowski M. P., et al., 2016, *ApJ*, 828, L21
- Koprowski M. P., Dunlop J. S., Michałowski M. J., Coppin K. E. K., Geach J. E., McLure R. J., Scott D., van der Werf P. P., 2017, arXiv/1706.0426,
- Kravtsov A. V., 2003, *ApJ*, 590, L1
- Kravtsov A. V., Klypin A. A., Khokhlov A. M., 1997, *ApJS*, 111, 73
- Kroupa P., 2002, *Science*, 295, 82
- Krumholz M. R., McKee C. F., Tumlinson J., 2009, *ApJ*, 699, 850
- Lacey C., Cole S., 1993, *MNRAS*, 262, 627
- Landsman W. B., 1993, in Hanisch R. J., Brissenden R. J. V., Barnes J., eds, *Astronomical Society of the Pacific Conference Series Vol. 52, Astronomical Data Analysis Software and Systems II*. p. 246
- Larson K. L., et al., 2016, *ApJ*, 825, 128
- Le Floch E., et al., 2005, *ApJ*, 632, 169
- Lin L., et al., 2008, *ApJ*, 681, 232
- Lintott C., et al., 2011, *MNRAS*, 410, 166
- Lotz J. M., Primack J., Madau P., 2004, *AJ*, 128, 163
- Lotz J. M., Jonsson P., Cox T. J., Primack J. R., 2008a, *MNRAS*, 391, 1137
- Lotz J. M., et al., 2008b, *ApJ*, 672, 177
- Lotz J. M., Jonsson P., Cox T. J., Primack J. R., 2010a, *MNRAS*, 404, 575
- Lotz J. M., Jonsson P., Cox T. J., Primack J. R., 2010b, *MNRAS*, 404, 590
- Lucy L. B., 1999, *A&A*, 344, 282
- Madau P., Dickinson M., 2014, *ARA&A*, 52, 415
- Marigo P., Girardi L., 2007, *A&A*, 469, 239
- Marigo P., Girardi L., Bressan A., Groenewegen M. A. T., Silva L., Granato G. L., 2008, *A&A*, 482, 883
- Michałowski M. J., et al., 2017, *MNRAS*, 469, 492
- Mihos J. C., Hernquist L., 1996, *ApJ*, 464, 641
- Muratov A. L., Kereš D., Faucher-Giguère C.-A., Hopkins P. F., Quataert E., Murray N., 2015, *MNRAS*, 454, 2691
- Narayanan D., Hayward C. C., Cox T. J., Hernquist L., Jonsson P., Younger J. D., Groves B., 2010a, *MNRAS*, 401, 1613
- Narayanan D., et al., 2010b, *MNRAS*, 407, 1701
- Narayanan D., Krumholz M., Ostriker E. C., Hernquist L., 2011, *MNRAS*, 418, 664
- Narayanan D., Krumholz M. R., Ostriker E. C., Hernquist L., 2012, *MNRAS*, 421, 3127
- Narayanan D., et al., 2015, *Nature*, 525, 496
- Narayanan D., Dave R., Johnson B., Thompson R., Conroy C., Geach J. E., 2017, arXiv/1705.05858,
- Robertson B., Cox T. J., Hernquist L., Franx M., Hopkins P. F., Martini P., Springel V., 2006a, *ApJ*, 641, 21
- Robertson B., Hernquist L., Cox T. J., Di Matteo T., Hopkins P. F., Martini P., Springel V., 2006b, *ApJ*, 641, 90
- Robitaille T. P., 2011, *A&A*, 536, A79
- Rodighiero G., et al., 2011, *ApJ*, 739, L40
- Rujopakarn W., et al., 2016, *ApJ*, 833, 12
- Sanders D. B., Mirabel I. F., 1996, *ARA&A*, 34, 749
- Shapley A. E., 2011, *ARA&A*, 49, 525
- Smith D. J. B., Hayward C. C., Jarvis M. J., Simpson C., 2017, arXiv/1707.00694,
- Snyder G. F., Lotz J., Moody C., Peth M., Freeman P., Ceverino D., Primack J., Dekel A., 2015a, *MNRAS*, 451, 4290
- Snyder G. F., et al., 2015b, *MNRAS*, 454, 1886
- Somerville R. S., Davé R., 2014, arXiv/1412.2712,
- Somerville R. S., Davé R., 2015, *ARA&A*, 53, 51

- Speagle J. S., Steinhardt C. L., Capak P. L., Silverman J. D., 2014, *ApJS*, **214**, 15
- Springel V., 2005, *MNRAS*, **364**, 1105
- Springel V., Di Matteo T., Hernquist L., 2005a, *MNRAS*, **361**, 776
- Springel V., Di Matteo T., Hernquist L., 2005b, *ApJ*, **620**, L79
- Strauss M. A., et al., 2002, *AJ*, **124**, 1810
- Tacconi L. J., et al., 2008, *ApJ*, **680**, 246
- Teyssier R., Chapon D., Bournaud F., 2010, *ApJ*, **720**, L149
- Thompson R., 2015, SPHGR: Smoothed-Particle Hydrodynamics Galaxy Reduction, Astrophysics Source Code Library (ascl:1502.012)
- Thompson R., Davé R., Huang S., Katz N., 2015, preprint, ([arXiv:1508.01851](https://arxiv.org/abs/1508.01851))
- Torrey P., et al., 2015, *MNRAS*, **447**, 2753
- Turk M. J., Smith B. D., Oishi J. S., Skory S., Skillman S. W., Abel T., Norman M. L., 2011, *ApJS*, **192**, 9
- Veilleux S., Kim D.-C., Sanders D. B., 2002, *ApJS*, **143**, 315
- Vladilo G., 1998, *ApJ*, **493**, 583
- Wadsley J. W., Stadel J., Quinn T., 2004, *New Astron.*, **9**, 137
- Watson D., 2011, *A&A*, **533**, A16
- Weingartner J. C., Draine B. T., 2001, *ApJ*, **548**, 296
- Whitaker K. E., van Dokkum P. G., Brammer G., Franx M., 2012, *ApJ*, **754**, L29
- White S. D. M., Rees M. J., 1978, *MNRAS*, **183**, 341
- Wuyts S., Cox T. J., Hayward C. C., Franx M., Hernquist L., Hopkins P. F., Jonsson P., van Dokkum P. G., 2010, *ApJ*, **722**, 1666
- Younger J. D., Hayward C. C., Narayanan D., Cox T. J., Hernquist L., Jonsson P., 2009, *MNRAS*, **396**, L66
- van der Walt S., Colbert S. C., Varoquaux G., 2011, *Computing in Science & Engineering*, **13**, 22

APPENDIX A: DIRECT METHOD COMPARISON

As a first test of our modeling methods, we examine the g3iso simulation from the ‘‘Dusty Interacting Galaxy GADGET-SUNRISE Simulations’’ (DIGGSS) simulation series¹⁰, and compared them with the reported values available with the mock observations of the simulations.

Here, we start with the sky subtracted observations and detection segmentation maps supplied with the catalogues. Like in the procedure outlined in Lotz et al. (2008a), we find the centre by minimizing the second-order moment of the central galaxy’s pixels, and determined the properties of the best fit ellipse using the algorithm implemented in the IDL task FIT_ELLIPSE (Fanning 2002). After this point we use the exact same procedure outlined earlier to compute r_p , a_p , C , A , G , and M_{20} are explained in 3.4.

Figures A1 and A2 illustrate the excellent agreement between the calculated and reported values of r_p , C , and A . In figures A1 and A3, slightly worse agreement is demonstrated for a_p , G , and M_{20} . Recall that we employ a different method to compute the value of a_p than was used to compute the tabulated values in the catalogue. As we will explain in § E, we conclude that our utilised method determines more accurate measurements of a_p for lower resolution observations. Therefore, we expect some modest deviations in the value of a_p , G , and M_{20} .

¹⁰ <http://archive.stsci.edu/prepds/diggss>

Table B1. The definitions for the times at which each merger stage begins are listed below. The actual calculated times for this idealized simulation are also listed. Each stage other than the ‘‘remnant’’ Stage includes all events from its starting time to the starting time of the next stage. The ‘‘remnant’’ stage includes all events after its start time.

Merger Stage	Definition	Time (Gyr)
Pre-Merger	0	0
First Pass	$0.5t_{fp}$	0.098
Max. Sep.	$0.5(t_{fp} + t_{max})$	0.284
Merger	$0.5(t_{max} + t_{merge})$	0.601
Post-Merger	$t_{merge} + 0.5$ Gyr	1.331
Remnant	$t_{merge} + 1.0$ Gyr	1.831

APPENDIX B: IDEALIZED MERGER COMPARISON

As a second check on the validity of the morphological measures, we compare the morphological measures of a galaxy merger in idealized simulation to the results found by Lotz et al. (2008a). In particular, we make use of the d4e simulation suite developed originally by Cox et al. (2006a,b) and Robertson et al. (2006a,b).

It is important to note a few minor differences between the mock observations generated for this comparison, and those for the cosmological zoom simulations that comprise our main study. Unlike the cosmological zoom simulations, these mock observations have been simulated at $\lambda = 4686$ Å to simulate the SDSS g filter (in order to best compare with Lotz et al. 2008a), and noise was added such that all pixels containing any projected stellar mass belonging to any galaxy had an $\langle SNR \rangle \sim 25$. Additionally, the binding lengths used for FOF halo and galaxy finding were slightly different from those used for the cosmological simulation. We set them both equal to 0.10 times the mean inter-particle distance as we found this greatly improved the ability of CAESAR to distinguish between the two galaxies in early merger stages.

These mock observations are simulated at an angular diameter distance of a galaxy at $z \sim 2$ where $0.05'' \sim 430$ pc. They have a pixel scale of $\sim 0.05'' \text{pixel}^{-1}$ and are convolved with a Gaussian of $FWHM \sim 0.15''$. Here, $0.05'' \sim 430$ pc. For comparison, the mock observations produced by Lotz et al. (2008a), have noise added slightly differently and the observations are simulated for SDSS at a distance where $0.396'' \sim 105$ pc. Those observations have a pixel scale $\sim 0.396'' \text{pixel}^{-1}$ and are convolved with a Gaussian of $FWHM \sim 1.5''$. One final difference from the analysis of the mock observations of the cosmological simulations is that we use a 9x9 tophat filter with a radius of 4.5 pixels during source detection; we found that this yielded better detection segmentation maps than those yielded by the 5x5 tophat filter with a radius of 2.5 pixels for the idealized simulation.

We classify the merger stages in a similar way to Lotz et al. (2008a). We determine t_{fp} , the time at which the galaxies are closest during their first pass, t_{max} , the time when the galaxies are the most separated and t_{merge} , the time at which the nuclei are merged (functionally, we determine this when the nuclear black hole sink particles in the two progenitors have merged). within 1 kpc of one another. Using these time-steps, we classify a galaxy’s merger stage into the

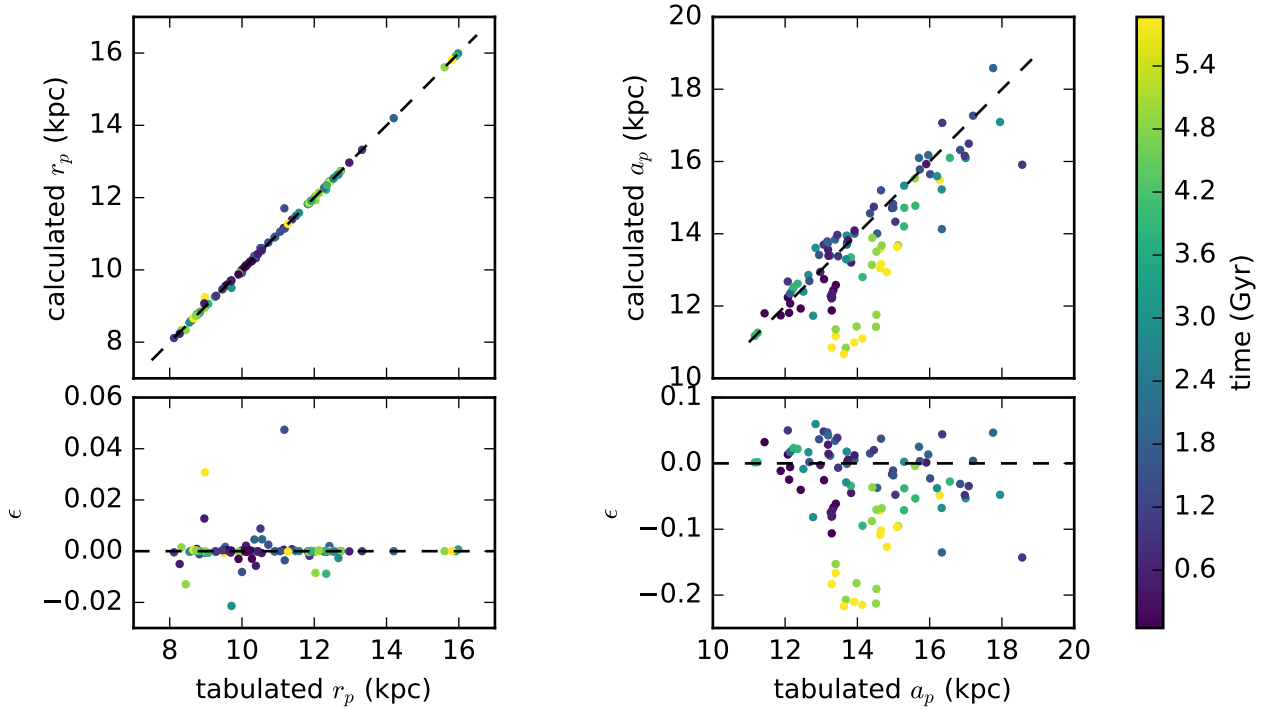


Figure A1. Comparison of the calculated r_p and a_p using methods described earlier in this paper with the tabulated values for the DIGGSS g3iso galaxy. In the lower panels, ϵ is the relative from the tabulated values. The symbol colours denote the simulation time.

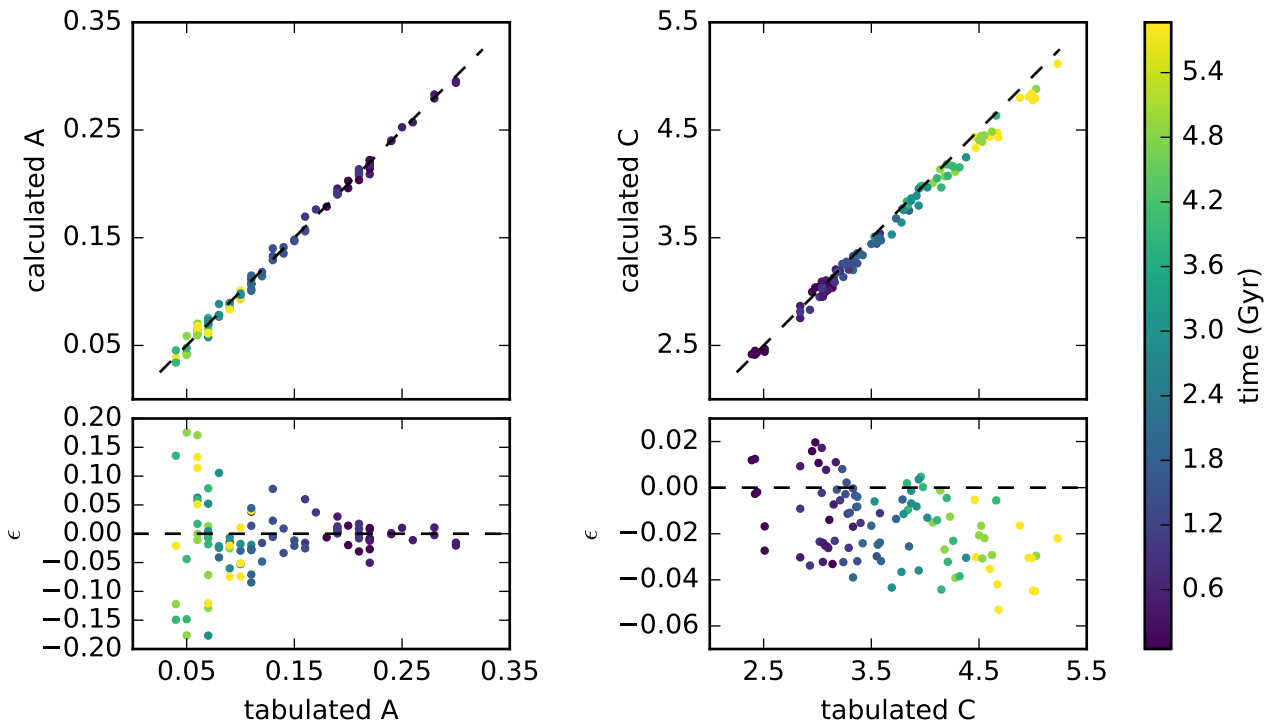


Figure A2. Comparison of the calculated A and C using methods described earlier in this paper with the tabulated values for the DIGGSS g3iso galaxy. In the lower panels, ϵ is the relative from the tabulated values. Symbol colours denote the simulation time.

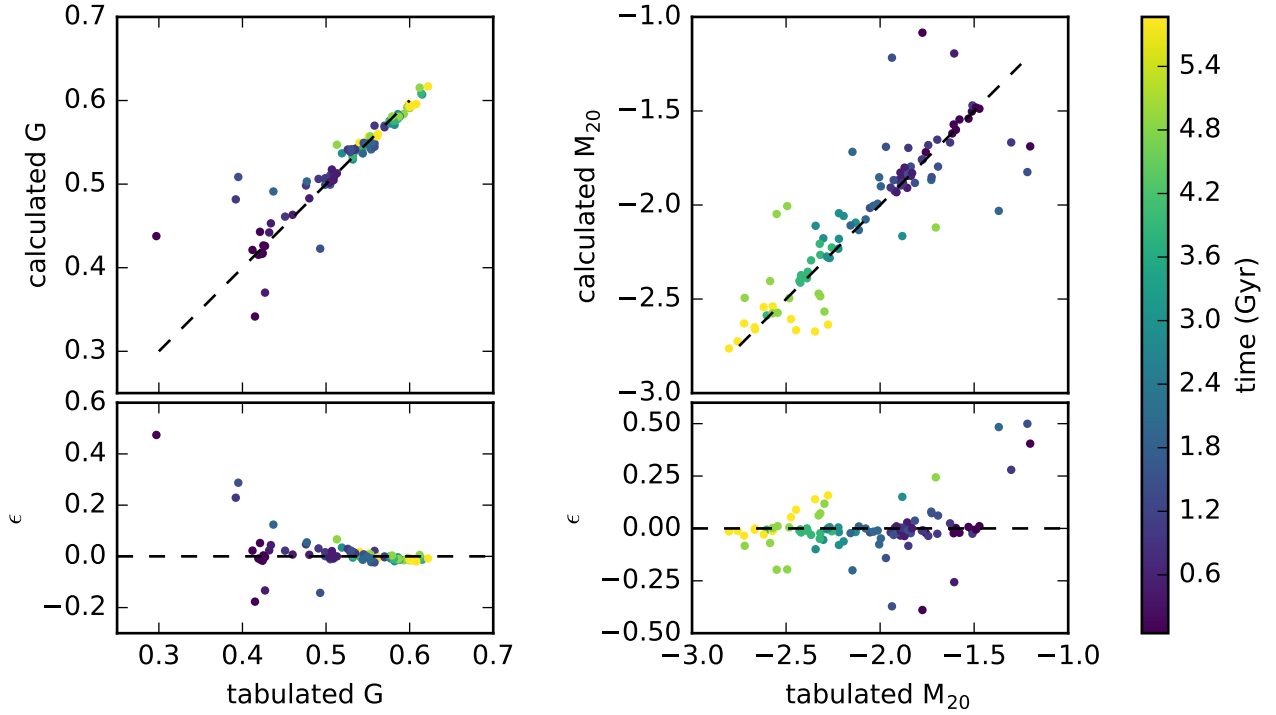


Figure A3. Comparison of the calculated G and M_{20} using methods described earlier in this paper with the tabulated values for the DIGGSS $g3iso$ galaxy. In the lower panels, ϵ is the relative from the tabulated values. Symbol colours denote the simulation time.

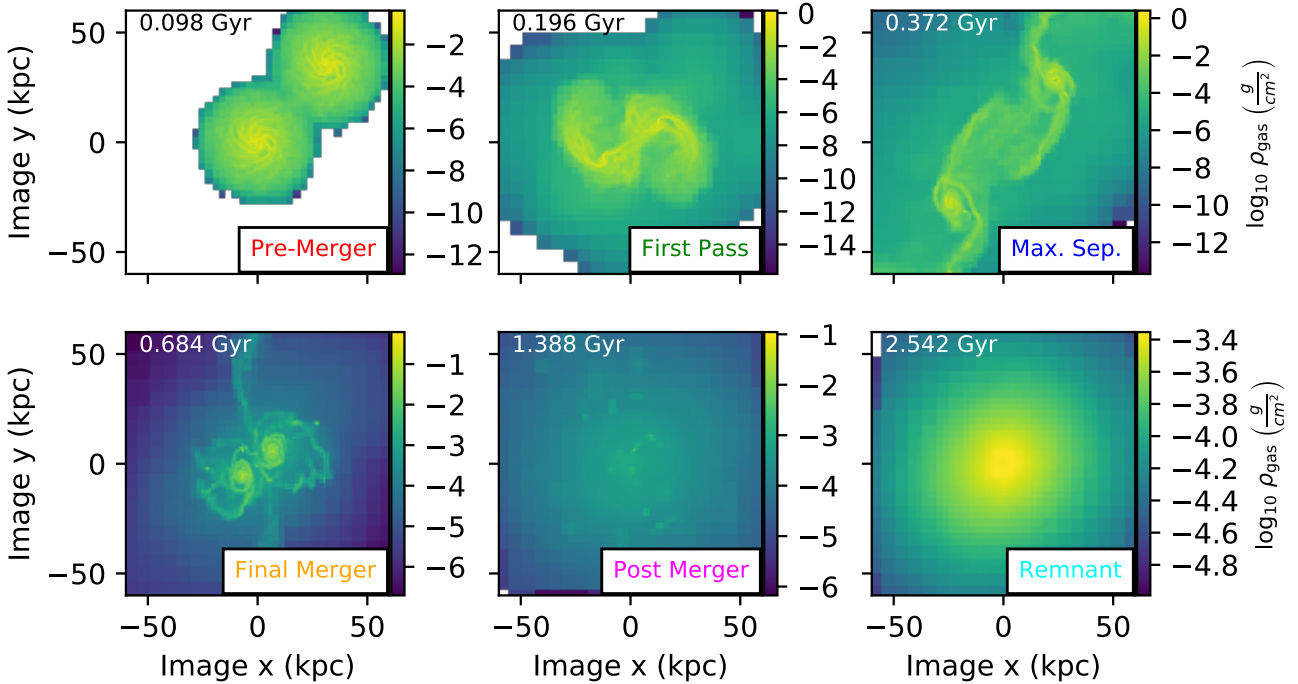


Figure B1. Gas surface densities of snapshots from each merger stage. Each panel is labelled with its associated merger stage in the lower right corner and the time since the simulation started in the upper left corner. The time periods for each merger stage are given in Table B1.

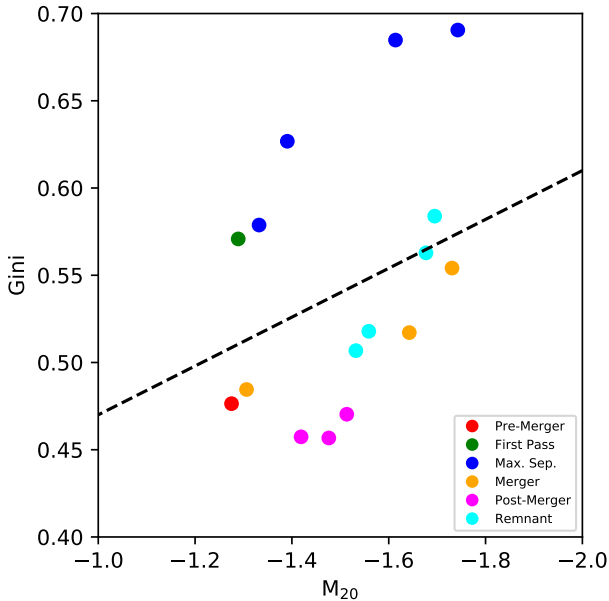


Figure B2. $G - M_{20}$ plot for select snapshots of the d4e idealized simulation. The points are the average G and M_{20} over all unique inclinations in a given snapshot. Points are coloured by the merger stage. The stages pre-merger, first pass, maximal separation, final merger, post merger, and remnant are coloured red, green, blue, orange, magenta, and cyan

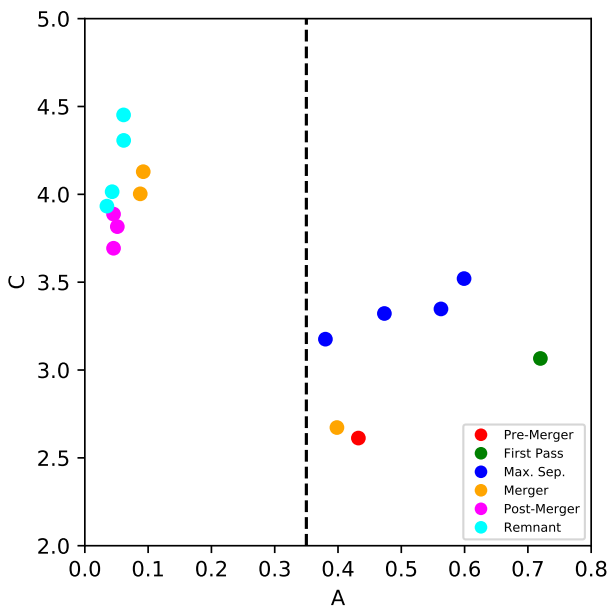


Figure B3. $C - A$ plot for select snapshots of the d4e idealized simulation. The points are the average C and A over all unique inclinations in a given snapshot. Like Figure B2, points are coloured by the merger stage.

following categories: 'pre-merger', 'first pass', 'maximal separation', 'merger', 'post-merger', and 'remnant'. See Table B1 for the definitions of the merger stages and Figure B1 for sample gas surface density plots in each merger stage.

Figures B2 and B3 show the average $G - M_{20}$ and $C - A$ values for select snapshots of the d4e simulation. The $G - M_{20}$ and $C - A$ values have been averaged over all unique

lines of sight at every snapshot. Note that no $\langle SNR \rangle$ cuts were made. Comparison of these results to those of (Lotz et al. 2008a) demonstrate that our image analysis methods yield comparable results to other image analysis methods.

APPENDIX C: ADDITIONAL POSTAGE STAMPS

Here, we include series of postage stamps analogous to Figure 5 for $mz5$, $mz10$, $mz45$, $mz287$, $mz352$, $mz374$ and $mz401$. In each Figure, we include snapshots close to $z \sim 5, 4, 3.5, 3, 2.5$ and 2 that all have valid A and $G - M_{20}$ along a consistent line of sight.

APPENDIX D: EFFECTS OF SELECTION CRITERIA ON UNCERTAINTY OF MERGER DIAGNOSTICS PERFORMANCE

Figure D1 illustrates the uncertainty in the performance of the merger diagnostics that results from our sample selection. The figure shows the most optimistic hypothetical true positive rates and false positive rates at any given potential timescale that the merger diagnostics could have if all of our data met our selection criteria.

APPENDIX E: PETROSIAN SEMI-MAJOR AXIS

Here, we discuss our methodology of computing a_p , and compare it to the method employed by Lotz et al. (2008a). As discussed in §3.4.3, the method we use to compute a_p draws heavy inspiration from the method employed in the photometric pipeline of SDSS to compute r_p . For the sake of this discussion, we will refer to method we currently use as Method A and the method used by Lotz et al. (2008a) as Method B. As we will discuss, at our model resolution Method A returns somewhat more accurate results than method B. This owes to: (i) the exactness of the photometry and (ii) the spacing of the points on the light curves constructed by each method.

The photometry we use in Method A subsamples the flux of pixels partially enclosed by an annulus. For comparison, in the photometry employed in Method B subsampling is not used. Instead, the entire flux of the pixel is included or not included based on where the annulus passes through the centre of the pixel. In higher resolution images, where the features of galaxies are distributed over more pixels, we expect there to be minimal difference in the photometry. However in lower resolution images we expect the differences in the photometry to be more significant.

Likewise, we expect the differences in the spacing of the points on the light profiles constructed by each method to have similar impacts on the accuracy of the recovered a_p at different image resolutions. In Method A the light profile is measured at exponentially spaced points. Near the centre of the galaxy, where features have a larger impact on the light profile (because they make up a larger fraction of the total enclosed flux), the light profile has sub-pixel spacing and further from the centre points on are spaced by more than a single pixel. In Method B, the light profile is measured

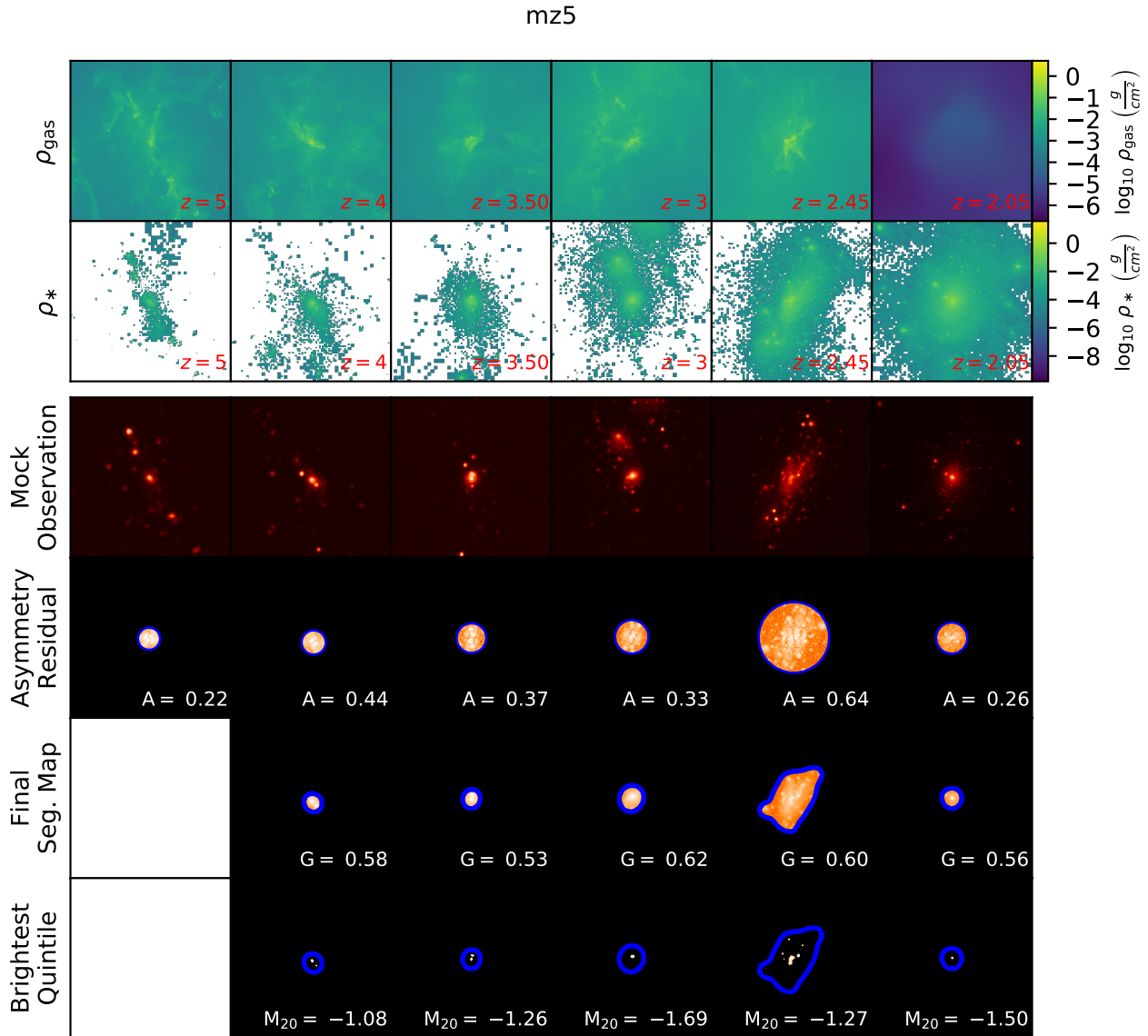


Figure C1. The same as Figure 5 except that the panels have correspond to the central galaxy of mz5, rather than that of mz0, and the panels are generated at $z \approx 5, 4, 3.5, 3, 2.6$ and 2.05 . The final segmentation map and brightest quintile has been omitted at the z when the final segmentation map has $\langle SNR \rangle < 20$ or is not contiguous.

at points with constant 1 pixel spacing. For low resolution images, we expect Method A to recover more accurate measurements as the features of the galaxy are condensed over a smaller number of pixels. However, for higher resolution images, we expect either minimal differences in the accuracy or that Method B might have better accuracy as it constructs the light profile with more finely spaced points at large distances.

In order to compare the performance of the methods, we used the exact Lotz et al. (2008a) methodology, and re-computed the a_p , G , and M_{20} for the the d4e idealized simulation and the g3iso simulation from the DIGGSS simulation series. As a reminder, the values computed for the simulations using Method A, are described in appendices B and A, respectively. In Figure E1 we illustrate the average $G - M_{20}$ values calculated for the idealized d4e simulation

calculated with Method B. Comparing this to Figure B2, it is evident that Method A performs slightly better regarding the location of post-merger remnants in $G - M_{20}$ space. Similarly, Figures E2 and E3 illustrate the comparison of the values of a_p , G , and M_{20} , calculated using Method B, to the tabulated values for the g3iso DIGGSS simulation¹¹. For comparison, figures A1 and A3 illustrate the deviations of

¹¹ As an aside, the deviation in these values likely arises from differences in the implementation of Powell's method for minimization between the SCIPY function `fmin_powell` (Jones et al. 2001) and the IDL procedure `POWELL`. This difference likely causes slightly different centre to be determined while minimizing A and because this centre serves as an initial guess for using Powell's method to minimize M_{tot} , the effect is compounded for the G and M_{20} values.

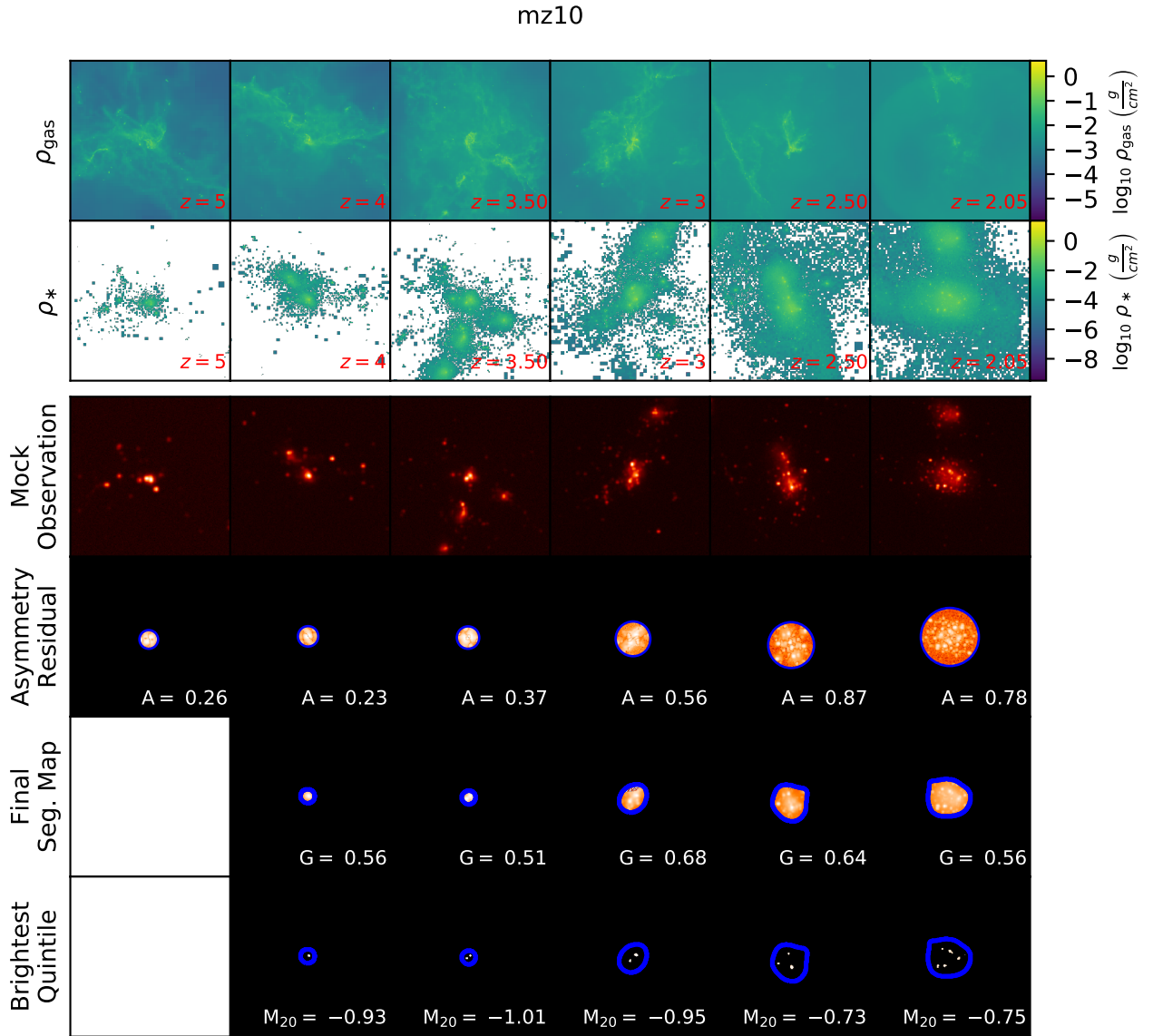


Figure C2. The same as Figure 5 except that the panels have correspond to the central galaxy of mz10, rather than that of mz0, and the panels are generated at $z \approx 5, 4, 3.5, 3, 2.5$ and 2.05 . The final segmentation map and brightest quintile has been omitted at the z when the final segmentation map has $\langle SNR \rangle < 20$ or is not contiguous.

the measurements calculated with Method A from the tabulated measurements. It is apparent that the measurements made with Method B are moderately closer to the tabulated values. However, because Method A recovers more accurate measurements at lower resolutions, we consider its deviations tolerable.

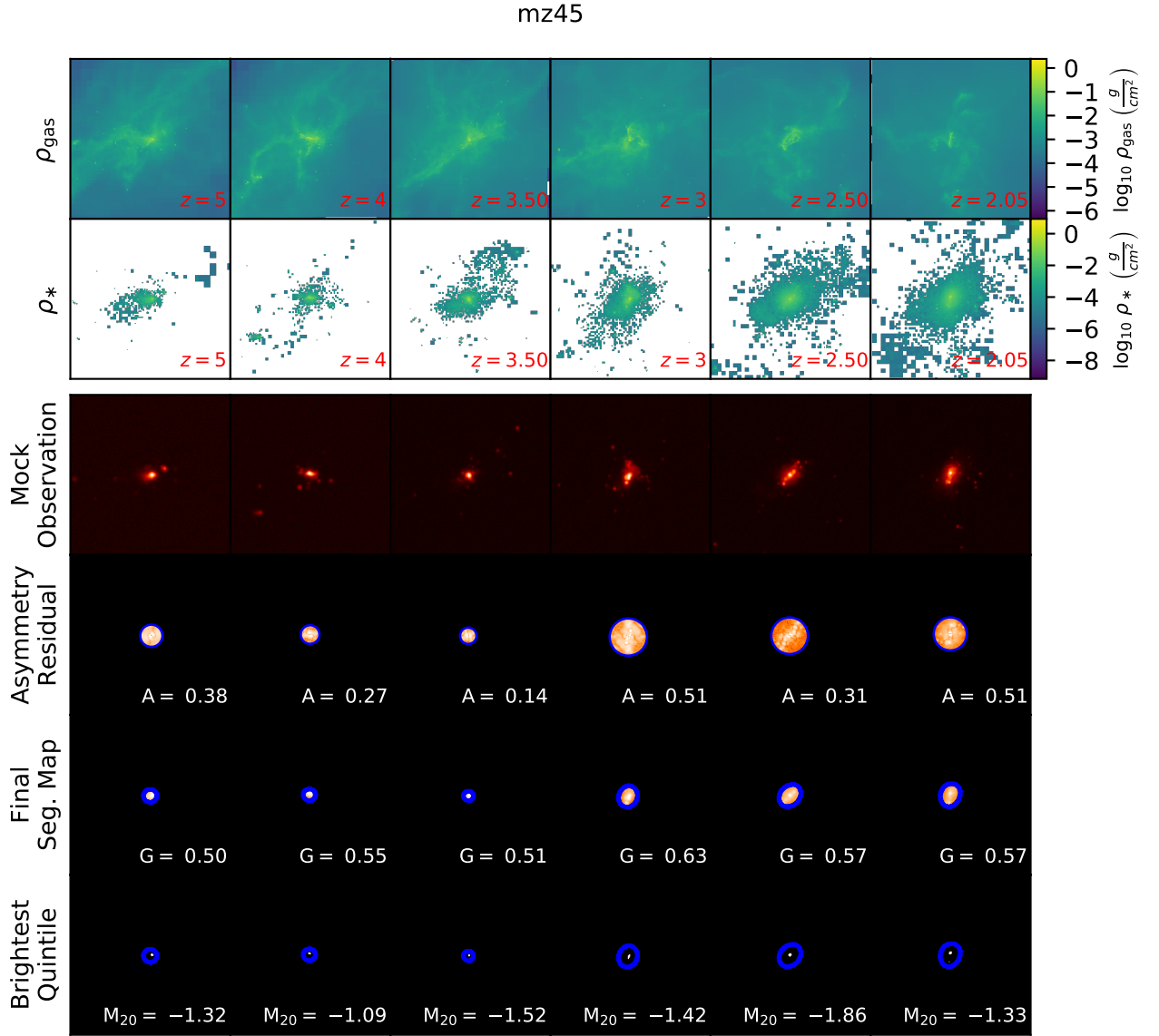


Figure C3. The same as Figure 5 except that the panels have correspond to the central galaxy of mz45, rather than that of mz0, and the panels are generated at $z \approx 5, 4, 3.5, 3, 2.5$ and 2.05 . The final segmentation map and brightest quintile has been omitted at the z when the final segmentation map has $\langle SNR \rangle < 20$ or is not contiguous.

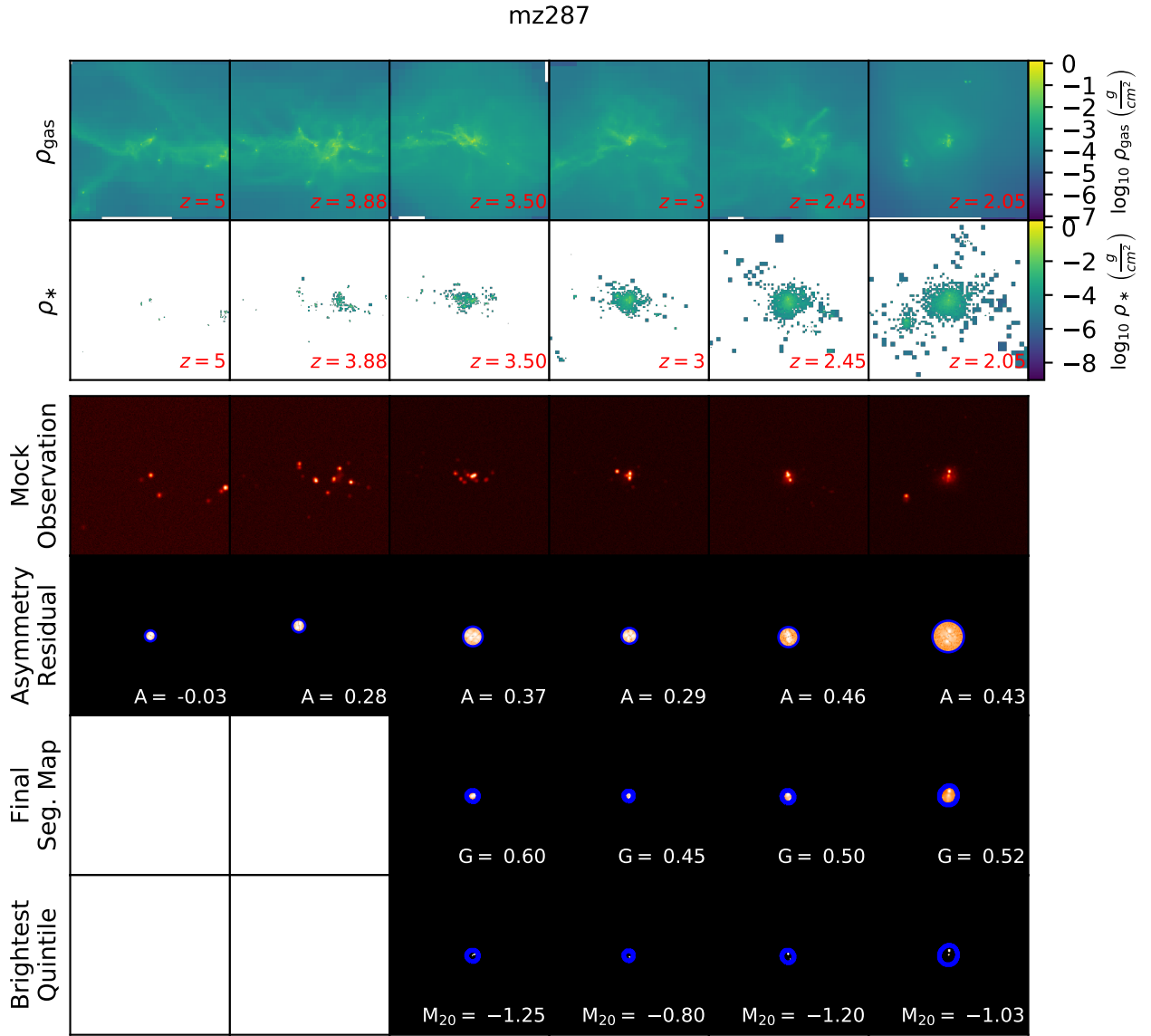


Figure C4. The same as Figure 5 except that the panels have correspond to the central galaxy of mz287, rather than that of mz0, and the panels are generated at $z \approx 5, 4, 3.5, 3, 2.5$ and 2.05 . The final segmentation map and brightest quintile has been omitted at the z when the final segmentation map has $\langle SNR \rangle < 20$ or is not contiguous.

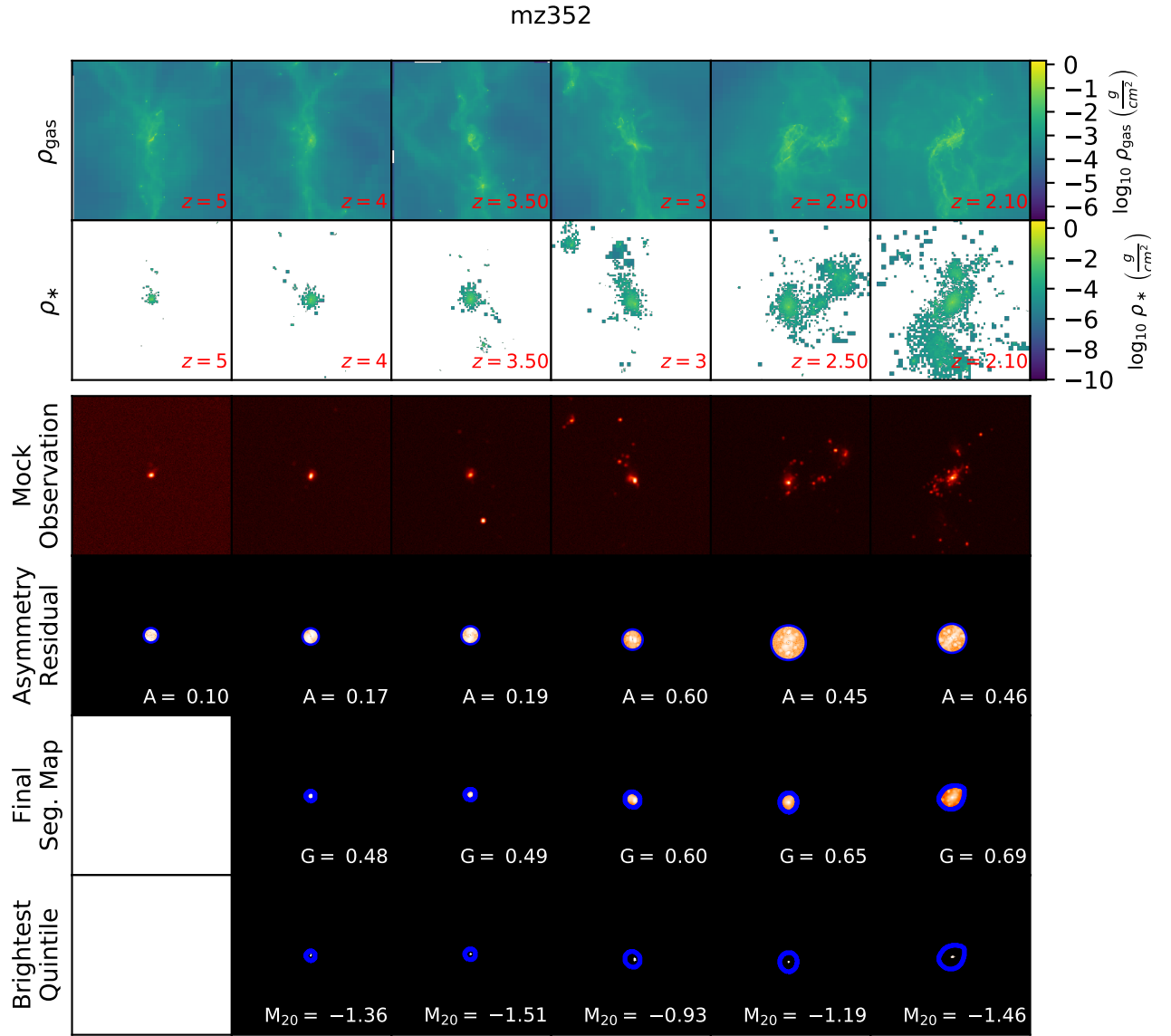


Figure C5. The same as Figure 5 except that the panels have correspond to the central galaxy of mz352, rather than that of mz0, and the panels are generated at $z \approx 5, 4, 3.625, 2.9, 2.45$ and 2.15 . The final segmentation map and brightest quintile has been omitted at the z when the final segmentation map has $\langle SNR \rangle < 20$ or is not contiguous.

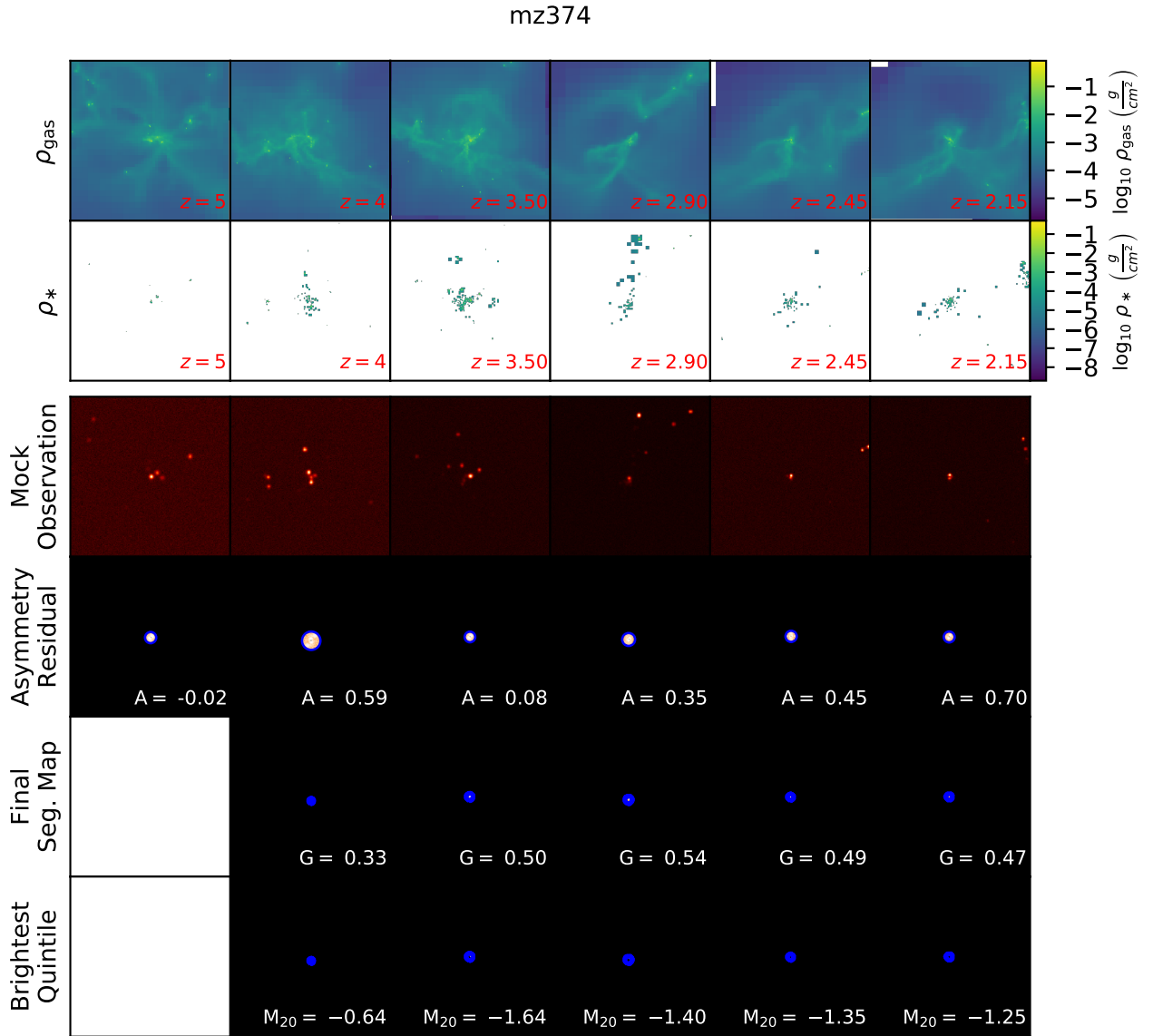


Figure C6. The same as Figure 5 except that the panels have correspond to the central galaxy of mz374, rather than that of mz0, and the panels are generated at $z \approx 5, 4, 3.5, 3, 2.45$ and 2.05 . The final segmentation map and brightest quintile has been omitted at the z when the final segmentation map has $\langle SNR \rangle < 20$ or is not contiguous.

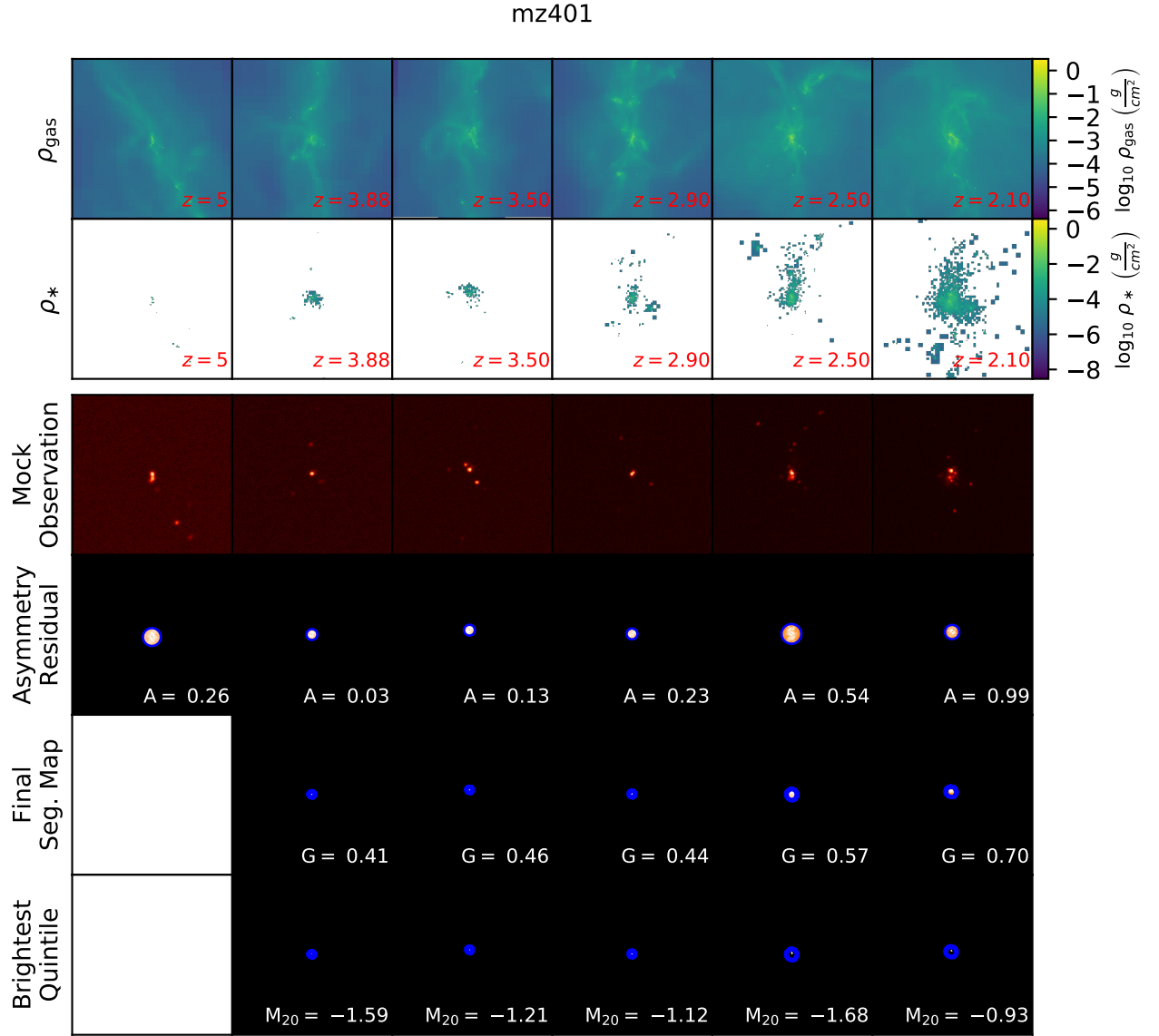


Figure C7. The same as Figure 5 except that the panels have correspond to the central galaxy of mz401, rather than that of mz0, and the panels are generated at $z \approx 5, 3.875, 3.5, 2.90, 2.5$ and 2.10 . The final segmentation map and brightest quintile has been omitted at the z when the final segmentation map has $\langle SNR \rangle < 20$ or is not contiguous.

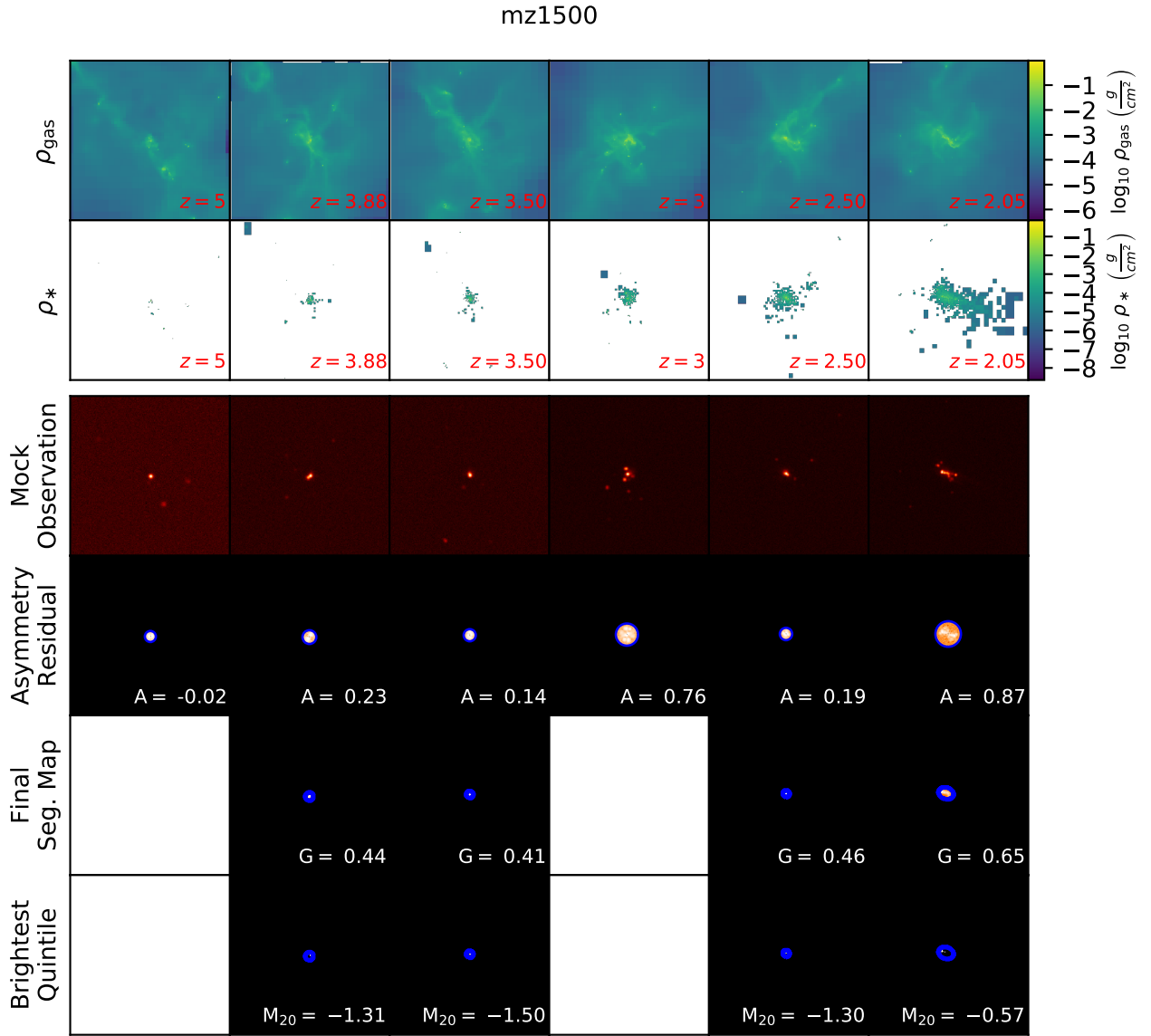


Figure C8. The same as Figure 5 except that the panels have correspond to the central galaxy of mz1500, rather than that of mz0, and the panels are generated at $z \approx 5, 3.875, 3.5, 3, 2.5$ and 2.05 . The final segmentation map and brightest quintile has been omitted at the z when the final segmentation map has $\langle SNR \rangle < 20$ or is not contiguous.

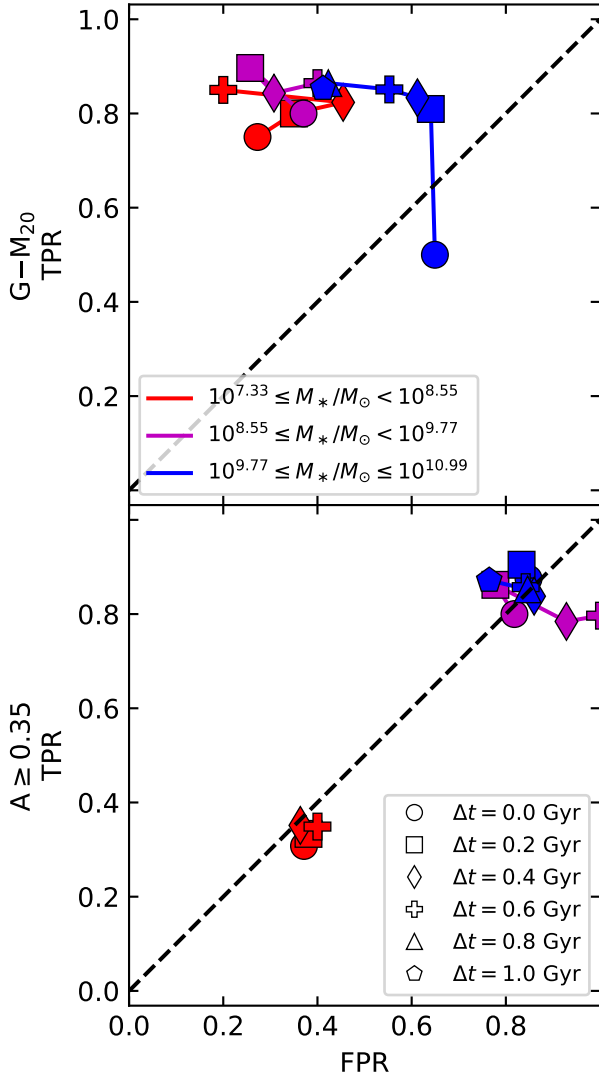


Figure D1. The same as Figure 12, but instead of ignoring the discarded data, at each possible Δt , $-\Delta t$ timescale we assume that all discarded data have values that maximize TPR and minimize FPR values.

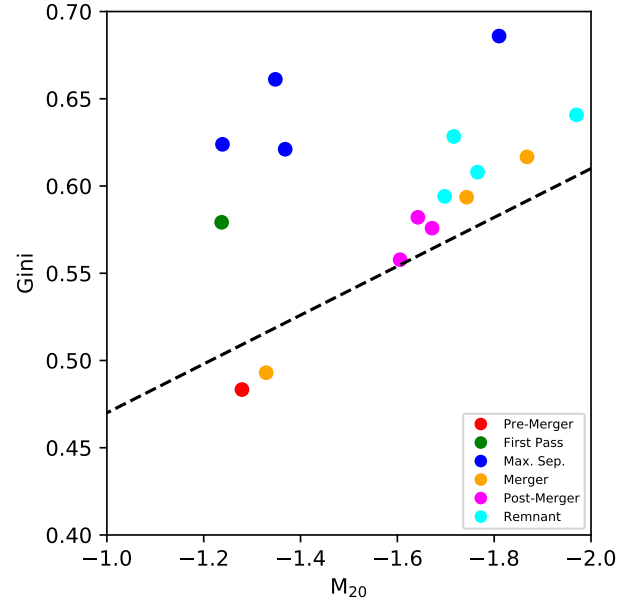


Figure E1. $G-M_{20}$ plot for select snapshots of the d4e idealized simulation produced when a_p is computed using the algorithm from Lotz et al. (2008a) (Method B). The data illustrated here can be directly compared against that featured in Figure B2.

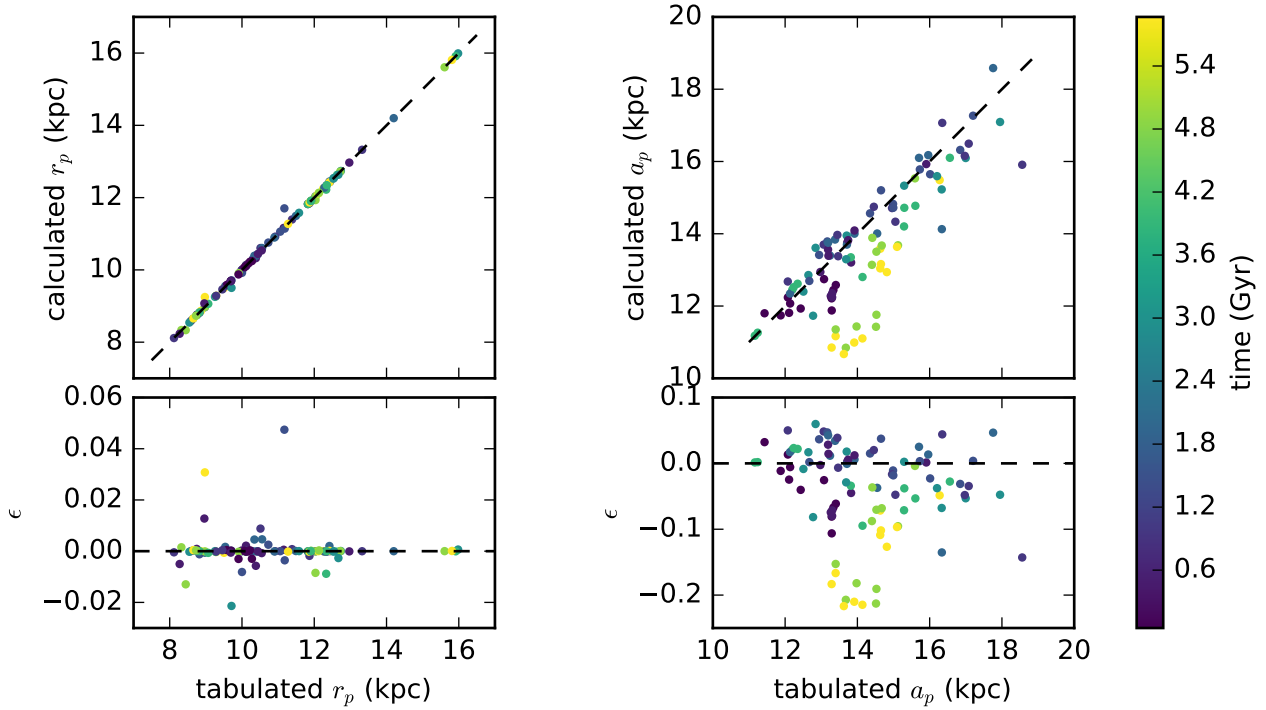


Figure E2. This is the same as figure A1 except that a_p values are computed with the algorithm used in Lotz et al. (2008a) (Method B).

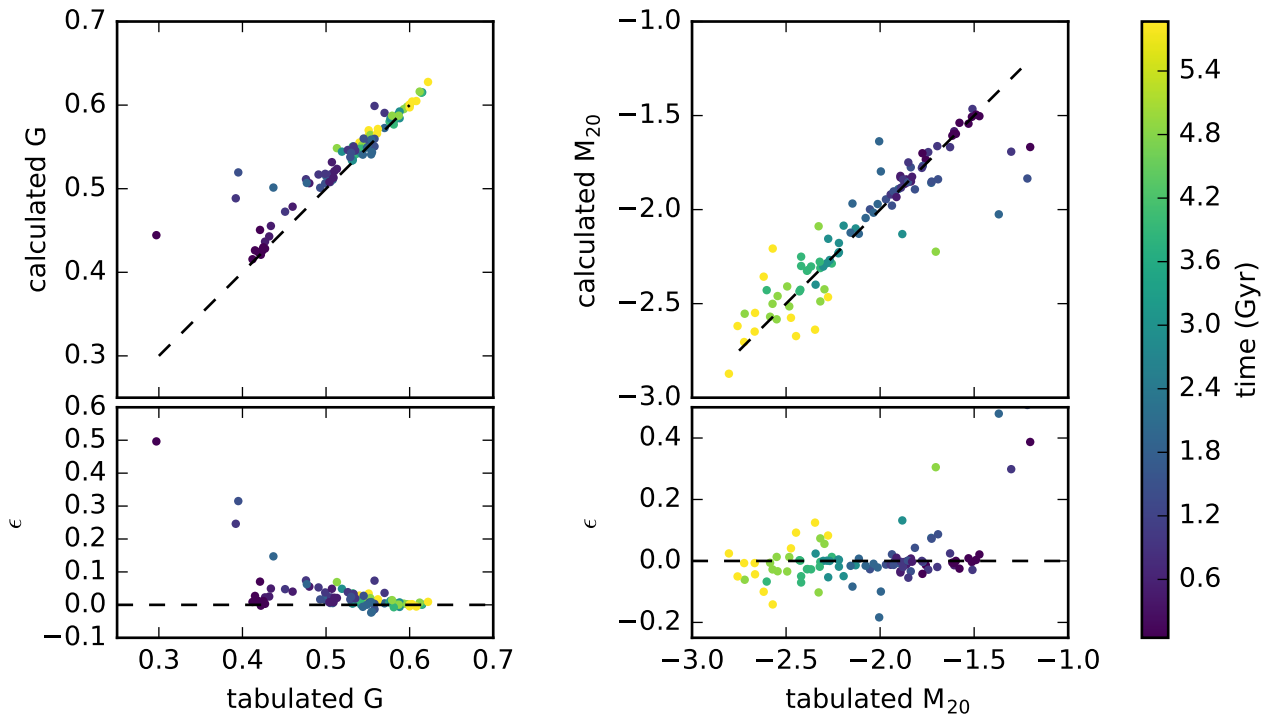


Figure E3. Comparison of the calculated G and M_{20} , using the values of a_p calculated with the algorithm employed in Lotz et al. (2008a) (Method B), with the tabulated values for the DIGGSS g3iso galaxy. In the lower panels, ϵ is the relative from the tabulated values. All points have been coloured by the time since the simulation started.